Check for updates

RESEARCH ARTICLE

NANO · MICRO small
www.small-journal.com

Strategic Core-Shell Integration for Advancing Z-Scheme Heterojunctions: Interface-Engineered $ZnIn_2S_4/Ag_2WO_4$@Ag Ternary Architecture for Enhanced Visible-Light-Driven Photocatalytic H_2 Production and Pollutant Degradation

Bharagav Urupalli, Dong-Seog Kim, Gi-Seung Shin, Geun-Jae Oh, Tuong Van Tran, Ji-Wook Yoon, and Yeon-Tae Yu**

The spatial inhomogeneity of interfacial modifications, despite conventional approaches like co-catalyst deposition and dopant incorporation, presents a critical bottleneck in achieving optimal charge carrier dynamics and sustained photocatalytic performance at semiconductor heterojunctions. To address this challenge, this study introduces a novel approach by encapsulating the wide-bandgap semiconductor Ag_2WO_4 (AWO) in a particulate shell of plasmonic hot spots (metallic Ag), forming a well-defined interface that facilitates consistent charge transfer and enhances photocatalytic efficiency. The engineered Ag_2WO_4@Ag (AWO@Ag) is strategically integrated with $ZnIn_2S_4$ (ZIS) nanosheets to design core–shell integrated Z-scheme heterojunction. The optimized integration of AWO@Ag (12.5%) over ZIS nanosheets demonstrates a remarkable hydrogen generation performance, achieving 3142 µmol $h^{-1}g^{-1}$, surpassing the performance of pure $ZnIn_2S_4$ (1311 µmol $h^{-1}g^{-1}$). Through rational interface design with strong redox abilities, the system achieves an impressive methyl orange photodegradation efficiency of 97.16% within 60 min. Additionally, it exhibits photoanodic currents of 3.98 mA cm^{-2} at 2.2 V versus RHE in a neutral electrolytic medium, demonstrating enhanced water oxidation capability facilitated by AWO@Ag integration. The system's exceptional performance across hydrogen generation, dye degradation, and water oxidation, validates that this advanced structural design enables stable and sustained photocatalytic performance through its multifunctional properties.

1. Introduction

Light-driven intensification of chemical reactions through photocatalysis provides a versatile platform for clean energy generation and environmental remediation.[1] Photocatalytic hydrogen production and organic pollutant degradation represent two critical applications of semiconductor photocatalysts that address pressing environmental and energy challenges.[2,3] The simultaneous pursuit of efficient water splitting for clean fuel generation and the mineralization of toxic organic contaminants reflects the dual environmental benefits these systems can provide. Both processes rely on similar fundamental principles of light absorption and charge carrier dynamics, yet each demands specific material characteristics for optimal performance. However, optimizing photocatalytic degradation efficiency of organic pollutants, particularly industrial dyes, still requires thorough understanding of charge transfer mechanisms and radical generation pathways to design high-performance photocatalytic systems.[4,5] The development of visible light-responsive semiconductors with high crystallinity, efficient charge carrier generation, separation, and transport, along with physicochemical stability, is the need of the hour.[6,7] Such targeted design of ideal semiconductor photocatalysts can lead to the creation of multifunctional materials with a cluster of applications.[8] In this context, researchers have tailored and utilized diverse materials, such as metal oxides, metal sulfides, metallic and non-metallic nitrides, perovskites, and metal–organic frameworks (MOFs) for energy and environmental applications.[9,10] Among these materials, metal sulfides generally exhibit lower bandgaps due to the smaller electronegativity difference between the metal and sulfur atoms, resulting in a weaker ionic character in the M-S bond compared to the M-O bond.[11] This weaker ionic character induces a narrow bandgap and facilitates easier electron excitation under visible light. The surface defects in sulfide-based materials also promote plasmon resonance effects in copper-containing variants, enabling

B. Urupalli, D.-S. Kim, G.-S. Shin, G.-J. Oh, T. Van Tran, J.-W. Yoon, Y.-T. Yu
Division of Advanced Materials Engineering
Research centre for Advanced Materials Development
eonbuk National University
Jeonju 54896, South Korea
E-mail: jwyoon@jbnu.ac.kr; yeontae@jbnu.ac.kr

The ORCID identification number(s) for the author(s) of this article can be found under https://doi.org/10.1002/smll.202501833

DOI: 10.1002/smll.202501833

 © 2025 Wiley-VCH GmbH

broad-spectrum light harvesting from UV to near-infrared regions.[10,12] Materials, such as $Zn_xCd_{1-x}Se$ and CuS, exhibit narrow bandgaps (typically 1.2–3.0 eV) that enable efficient visible light absorption, making them far more practical than traditional wide bandgap photocatalysts.[13]

$ZnIn_2S_4$ (ZIS) is a proven photocatalyst with a visible light-responsive bandgap and a conduction band edge potential more negative than the H^+/H_2 redox potential, making it suitable for photocatalytic hydrogen evolution.[14] Compared to some well-known candidates such as CdS, MoS_2, and Bi_2S_3,[15] the photocatalytic H_2 production and dye degradation rates of pristine ZIS are higher and reproducible.[16,17] Witnessing these benefits, ZIS has emerged as one of the prominent semiconductors for photocatalytic applications. While ZIS demonstrates exponential performance gains through recent advancements, swift electron–hole recombination, sulfur instability, and limited oxidation potential remain major challenges.[14] To address these limitations, elemental doping, defect engineering, and surface modification strategies have been performed over ZIS.[18] Additionally, ZIS integration with diverse heterojunction counterparts and co-catalysts has been explored to achieve remarkable redox capabilities.[19–21] Some of the recent advancements in this direction include Pt-loaded ZIS nanoflowers,[22] WO_3@ZIS core–shell heterojunctions,[23] N-doped ZIS[24] and Ce-doped ZIS.[25]

Therefore, developing a holistic approach to enhance ZIS oxidation capability and photo-stability remains a top priority. In a recent report, Niu et al. demonstrated that the rational design of Z-scheme heterojunctions containing a strong and suitable oxygen evolution photocatalysts (OEPs) exhibits the best charge transfer pathways among all those reported to date.[26] The uniqueness of Z-scheme lies in its capability to facilitate intrinsic charge carrier distribution through internal electric fields across strong reduction and oxidation-capable components, thereby successfully suppressing charge carrier recombination, reducing photo-corrosion, lowering overpotential, and extending material selectivity.[3,27] Unlike type II heterojunctions where charge carriers move to less reactive positions, Z-scheme charge dynamics direct electrons and holes to the most catalytically favorable active sites for enhanced photocatalytic efficiency.[10] This charge transfer pathway involves the recombination of less reactive carriers at the heterojunction interface, specifically electrons from the conduction band of one semiconductor with holes from the valence band of another. The remaining highly reductive electrons and strongly oxidative holes are then available for important photocatalytic redox reactions.[28] The successful construction of Z-scheme heterojunctions requires precise band engineering, where the energy levels of the participating semiconductors must be appropriately aligned to facilitate the desired charge transfer dynamics.[5] Additionally, the interface quality, internal electric field formation, and band bending play crucial roles in establishing the unidirectional electron flow that characterizes Z-scheme systems. Since ZIS inherently responds to visible light, the addition of a semiconductor with bandgap higher than 3.1 eV offers more advantages than the addition of materials with the same bandgaps (2.2–2.5 eV). This innovative strategy creates a path to utilize wide bandgap semiconductors while generating a strong oxidation region in the system. The construction of diverse heterojunctions using wide-bandgap semiconductors represents an innovative approach to expand the spectral response range and advance light-driven technologies. To date, ZIS has been paired with a limited number of wide-bandgap semiconductors, such as ZnS, ZnO, and $ZnWO_4$, etc.,[29,30] which have created transformative research opportunities in the field of water splitting. $Ag_2WO_{4\ is}$ one such wide bandgap semiconductor, which is known to have a tunable wide bandgap, high crystallinity, and long-lasting physicochemical stability.[31,32] Recent reports on silver, silver tungstate-based binary and ternary combinations such as $Ag_2WO_4/Ag/Bi_2MoO_6$,[33] WO_3/Ag_2WO_4,[34] AgI/Ag_2WO_4,[35] $ZnO/Ag/Ag_2WO_4$,[36] g-C_3N_4/Ag_2WO_4,[37–39] and $MnWO_4/Ag_2WO_4$[40] evident the potential of Ag_2WO_4 for dye degradation and CO_2 reduction applications. The aforementioned studies utilized silver (Ag) as a mediator across heterojunction components. However, this incorporation involves the random distribution of silver nanoparticles on the semiconductor surface. The nonuniform and intermittent deposition of silver co-catalyst on Ag_2WO_4, characterized by sparse surface loading and insufficient interfacial contacts, compromises the overall system performance and diminishes the effectiveness of Ag_2WO_4 inclusion. To address these challenges, in this study, a particulate silver layer was formed as a shell on Ag_2WO_4 to maintain constant surface contact with Ag_2WO_4 while maintaining the visible spectral response and catalytic activity.

Considering the outstanding properties of Ag_2WO_4 and Z-scheme compatibility of ZIS, a synergistic architecture was designed via Ag shelling to effectively utilize the collective redox abilities. In this study, an advanced Z-scheme heterojunction, Ag_2WO_4@Ag/$ZnIn_2S_4$, was strategically developed by incorporating a particulate Ag shell on the surface of Ag_2WO_4 core. The optimized ternary photocatalyst, AAZ-3, not only addresses the major limitations of pristine ZIS but also achieves superior and sustained photocatalytic and photoelectrochemical performance. We report the first demonstration of strategic silver (Ag) shelling that significantly enhances visible light absorption of wide bandgap AWO through plasmonic resonance-induced hot electron injection, forming an efficient semiconductor core-metallic particulate shell integrated Z-scheme heterojunction. Comparative studies of photocatalytic hydrogen production, dye degradation, and photoelectrochemical water splitting demonstrate the improved performance of optimized ternary composite AWO@Ag/ZIS over that of binary AWO/ZIS and ternary Ag-loaded AWO/ZIS systems. Notably, this system exhibits excellent recyclability and sustained photocatalytic performance in long run over five cycles, suggesting a promising strategy for developing next-generation multifunctional Z-scheme heterojunctions.

2. Results and Discussion

A detailed structural analysis was conducted on ternary composites (AAZ specimens) to comprehensively understand their physicochemical properties comprehensively. The thorough investigations included assessments of crystallinity, purity, band structures, morphological interactions, elemental oxidation states, and the charge carrier dynamics of the heterostructures. Furthermore, the band structures of pristine ZIS and AWO were estimated to gain insight into the plausible reaction mechanisms for dye degradation and hydrogen production. Prior to the structural characterization of ternary composites, parent AWO,

© 2025 Wiley-VCH GmbH

16136829, 2025, 34, Downloaded from https://onlinelibrary.wiley.com/doi/10.1002/smll.202501833 by Jeonbuk National University, Wiley Online Library on [18/10/2026]. See the Terms and Conditions (https://onlinelibrary.wiley.com/terms-and-conditions) on Wiley Online Library for rules of use; OA articles are governed by the applicable Creative Commons License

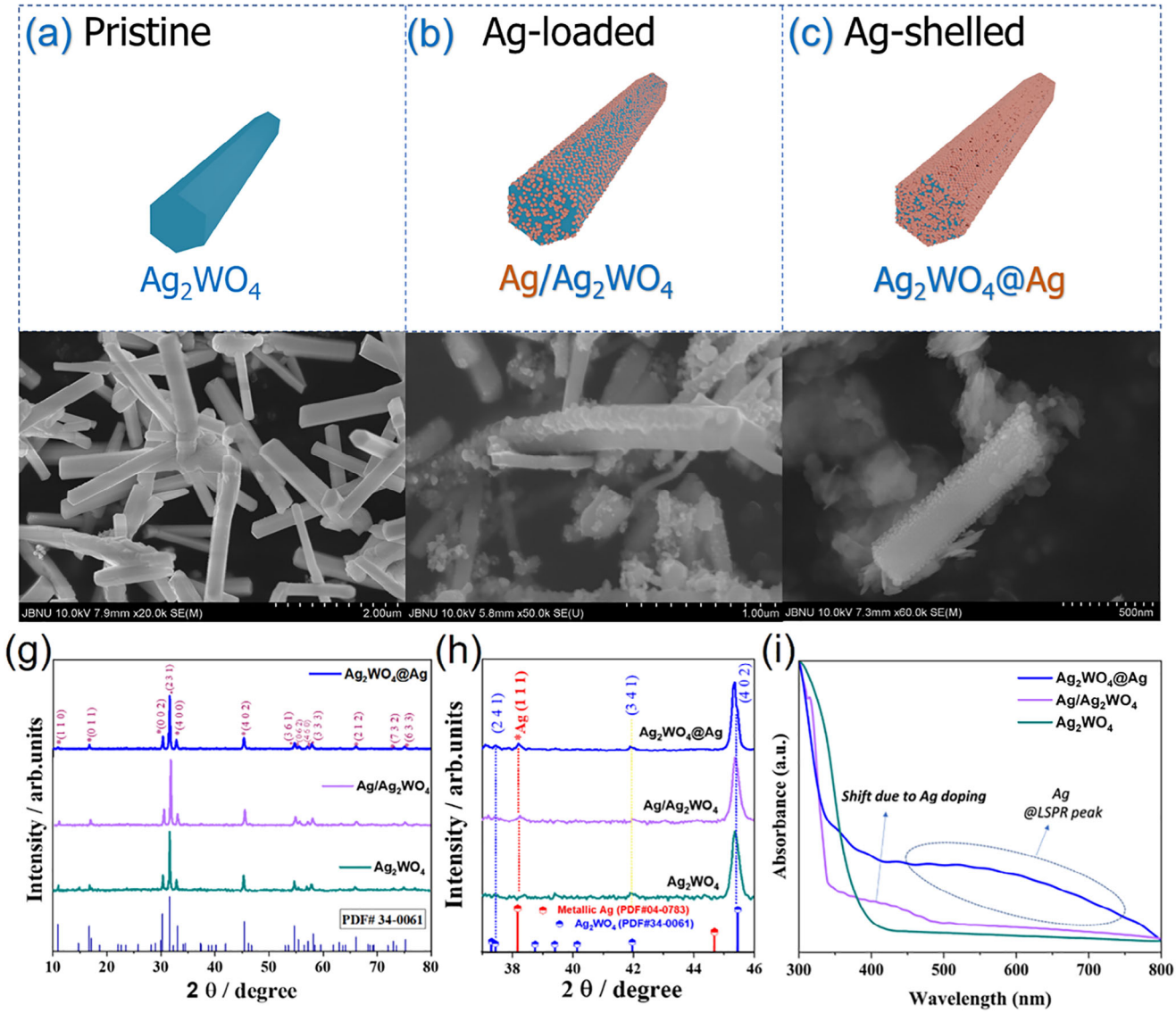


Figure 1. Pictorial depiction of pristine a) Ag_2WO_4 (AWO) hexagonal rods, b) Ag loaded Ag_2WO_4 (Ag/AWO) and c) Ag shelled Ag_2WO_4 (AWO@Ag), d–f) FE-SEM images for Ag_2WO_4, Ag/ Ag_2WO_4 and Ag_2WO_4@Ag. g) XRD Patterns of different AWO specimens collected at high scan rates h) XRD patterns collected Low scan (0.05° increment in 2θ) rates for the detection of Ag NPs from 37 to 40°. i) UV Vis absorbance spectra of Ag doped, Ag shelled Ag_2WO_4 and pristine Ag_2WO_4.

Ag-loaded AWO (Ag/AWO), and Ag-shelled AWO (AWO@Ag) were characterized in detail using XRD (high and low scan rates), FE-SEM, and UV Vis absorption spectroscopy analysis and obtained results were presented in **Figure 1**.

Figure 1a–c depicts the schematic representations of hexagonal rods of Ag_2WO_4, Ag-loaded, and Ag-shelled Ag_2WO_4. The morphological evidences obtained from FE-SEM analysis served as a basis for these depictions. The bluish cyan hexagonal rod in Figure 1a represents pristine AWO, while the brownish-pink spheres sparsely loaded or uniformly shelled over the AWO rods illustrate the Ag-loaded AWO (Ag/AWO) and Ag-shelled AWO (AWO@Ag) composites, as shown in Figure 1b,c, respectively.

The FE-SEM micrographs of silver tungstate-based specimens AWO, Ag/AWO, and AWO@Ag are presented in Figure 1d–f respectively. The crystallographic patterns of pristine Ag_2WO_4 exhibited intense peaks associated at 2θ of 10.98, 16.71, 30.27, 31.63, 33.09, 45.45, 54.66, 55.41, 57.19, 58.15, 66.07 and 72.98°, which are attributed to their respective (110), (011), (002), (400), (402), (361), (062), (460), (333), (214) and (732) planes of orthorhombic phase (PDF#34-0061).[41] All these peaks were present in Ag/Ag_2WO_4 and Ag_2WO_4@Ag, as evidenced in Figure 1g, with no significant peak shifts. In order to attain deeper insights into silver nanoparticles presence on the surface of Ag_2WO_4 rods, X-ray diffraction analysis was further conducted at low scan rates (0.02° increment in 2θ) from 37° to 46°, and the resulting patterns were shown in Figure 1h. The metallic Ag peak associated with 38.2°, corresponding to the (111) plane (PDF#04-0783) of silver, confirms the presence of the surface-bound

© 2025 Wiley-VCH GmbH

16136829, 2025, 34, Downloaded from https://onlinelibrary.wiley.com/doi/10.1002/smll.202501833 by Jeonbuk National University, Wiley Online Library on [18/10/2026]. See the Terms and Conditions (https://onlinelibrary.wiley.com/terms-and-conditions) on Wiley Online Library for rules of use; OA articles are governed by the applicable Creative Commons License

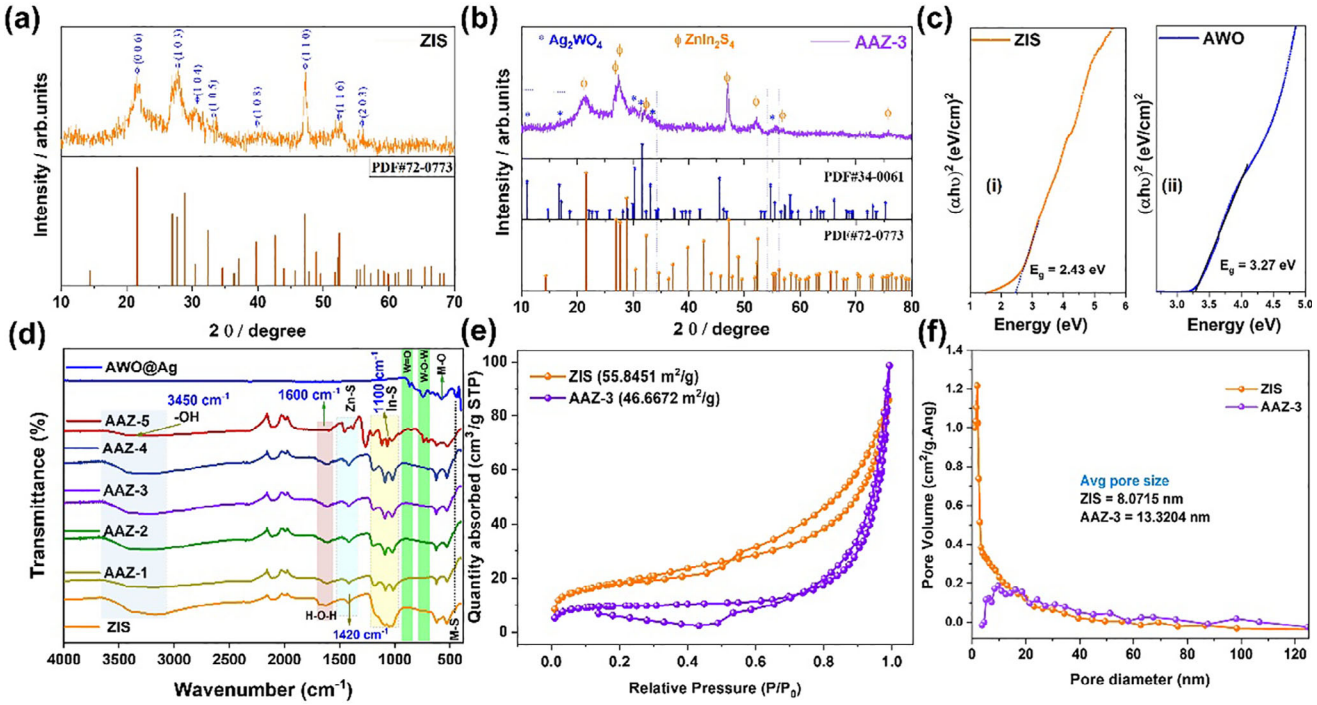


Figure 2. XRD patterns of a) ZIS, b) Optimized AWO@Ag/ZIS (AAZ-3), c) Kubleka Munk function derived bandgaps of ZIS and AWO, d) FTIR spectra of ZIS, AWO@Ag and AAZ-1,2,3,4 and 5 e) BET adsorption-desorption isotherms of ZIS and AAZ-3 f) BJH pore distribution curves if ZIS and AAZ-3.

metallic Ag in Ag-loaded and Ag-shelled Ag_2WO_4, while affirming the absence of external Ag in pure Ag_2WO_4 diffraction pattern. UV–vis absorption spectroscopy was employed to corroborate the structural analysis. The pristine Ag_2WO_4 exhibited an absorbance edge at 385 nm, whereas Ag/Ag_2WO_4 showed a notable red shift in absorption, extending into the visible region up to 500 nm. The Ag_2WO_4@Ag displayed a characteristic LSPR peak of metallic silver and a broad absorbance response across the visible region of the solar spectrum, as shown in Figure 1i.

The crystallographic pattern of pristine ZIS (**Figure 2a**) completely resembled the characteristic peaks of the hexagonal phase (PDF#72-0773).[42] Peaks with higher intensities identified at 21.58, 26.96, 27.69, 28.87, 32.37, 39.77, 42.656, and 47.176° correspond to the (006), (101), (102), (103) (105), (108), (109), (110) and (116) planes of ZIS. Figure 2b shows the XRD pattern of AAZ-3, which reveals the formation of a ternary composite with both AWO and ZIS planes. The crystallographic patterns of all the ternary composites AAZ1-5 are demonstrated in Figure S2 (Supporting Information). The distinct AWO@Ag peaks without any noticeable shifts in the ZIS pattern indicate the formation of a well-defined heterostructure. The peak of metallic Ag observed in Ag_2WO_4@Ag was indistinguishable in AAZ-3 because of its lower content and ZIS shielding. The absorbance spectrum of parent ZIS was demonstrated in Figure S3 (Supporting Information), the bandgap values of ZIS and AWO are derived using the Kubleka Munk function from the reflectance data of powder samples, and the bandgap energy values were determined to be 2.43 and 3.27 eV, respectively (Figure 2c). The prepared samples were further characterized for functional group analysis by FTIR, with the results shown in Figure 2d. AWO@Ag exhibits an intense stretching vibration of M-O (Ag-O of AWO) at ≈562 cm^{-1}, and W-O-W stretching at 737 cm^{-1} which corresponds to the WO_6 units within the Ag_2WO_4 crystal lattice. A less intense peak appeared at 864 cm^{-1} is attributed to the W═O weak bending vibration.[43] The FTIR spectra of the ZIS component in all the prepared samples align well with the previous reports.[44,45] Broad bands at 1100 cm^{-1} region depicts the In-S stretching vibrations and their interactions with the surrounded AWO molecules.[46] The weak bending modes present at 1420 and 1600 cm^{-1} in ZIS and composites spectra indicate the presence of Zn-S and water molecules (H-O-H) adsorbed on the surface. Additionally, the broad peak at ≈3400 cm^{-1} suggests the hydroxyl groups on the surface of the prepared photocatalysts.[47] These hydroxyl groups play a key role in enhancing the hydrophilicity of the catalyst surface.[48] As the AWO@Ag loading increases (from AAZ-1 to AAZ-5), the W—O—W and W═O octahedral stretching vibration becomes more evident in the AAZ-5 spectrum. This confirms the integration of AWO@Ag and ZIS in the final composite. Minor stretching peaks are observed starting from AAZ-2 in the highlighted region of Figure 2d. For AAZ-1, the W═O stretching is indistinguishable due to the small amounts of AWO@Ag loading. Figure 2e presents the N_2 adsorption-desorption isotherms of ZIS and champion ternary composite AAZ-3. The adsorption of both specimens is promoted at low relative pressure (P/Po) values from 0.5 to 1.0, depicting the type IV isotherm with an H3 hysteresis loop, which is indicative of non-uniform mesoporous distribution. The BET surface area of ZIS was calculated to be 55.84 $m^2\ g^{-1}$. A similar distribution trend was also reported with layer-by-layer stacked nanosheet morphology of ZIS.[49] However, the addition of 12.5 wt.% AWO@Ag to the ZIS (AAZ-3) exhibits a decrease in BET surface area value to 46.62 $m^2\ g^{-1}$. This decrement could be attributed to the shielding of the accessible surface

© 2025 Wiley-VCH GmbH

16136829, 2025, 34, Downloaded from https://onlinelibrary.wiley.com/doi/10.1002/smll.202501833 by Jeonbuk National University, Wiley Online Library on [18/10/2026]. See the Terms and Conditions (https://onlinelibrary.wiley.com/terms-and-conditions) on Wiley Online Library for rules of use; OA articles are governed by the applicable Creative Commons License

area of ZIS by loading AWO@Ag micro-rods. The abundance of functional groups on the surface of ZIS, compared to AAZ-3, corroborates the evidence for the higher surface area of ZIS. The BJH pore size distribution further affirms that the pore volume of AAZ-3 is reduced compared to ZIS, as shown in Figure 2f.[50] However, adding AWO@Ag improves the uniformity of pore diameter, and the average pore size was observed to increase for AAZ-3 (13.32 nm) compared to ZIS (8.07 nm). This increase in pore size within the mesoporous level can enhance the internal mass transport of reactants through diffusion on the catalyst surface, resulting in better water-splitting activity. Additionally, this phenomenon can enhance the accessibility of active sites for large dye molecules, resulting in improved dye degradation performance. The nitrogen adsorption-desorption isotherms and corresponding pore size distribution curves of AAZ series samples are presented in Figure S4 (Supporting Information). The specific surface areas of the samples are in the order of AAZ-1 (53.01 $m^2\ g^{-1}$), AAZ-2 (48.90 $m^2\ g^{-1}$), AAZ-3 (46.66 $m^2\ g^{-1}$), AAZ-4 (40.17 $m^2\ g^{-1}$), and AAZ-5 (33.11 $m^2\ g^{-1}$). All samples exhibit type IV isotherms with H3-type hysteresis loops, indicating the presence of mesoporous structures. The pore size distribution analysis reveals that AAZ-3 possesses a well-developed mesoporous structure with pore diameters primarily distributed between 2–20 nm, which facilitates efficient mass transport during photocatalytic reactions. Interestingly, while AAZ-1 has the highest surface area, it does not show the best photocatalytic performance, indicating that the enhanced activity of AAZ-3 stems primarily from its optimized electronic structure and Z-scheme charge transfer mechanism rather than surface area effects alone. We have incorporated this discussion in the revised manuscript to provide a more comprehensive understanding of our photocatalyst's properties.

Figure 3 presents the deconvoluted XPS spectra for ZIS, AWO@Ag, and AAZ-3 materials. The XPS survey spectra of ZIS, AWO@Ag, and AAZ-3 are presented in Figure S5 (Supporting Information). The XPS spectra of pristine ZIS and AAZ-3 exhibit characteristic doublets for each element Zn, In, and S,[51] following data fitting (Figure 3a–c). As illustrated in Figure 3a, the Zn 2p spectrum reveals two peaks at 1022.18 eV and 1045.28 eV, corresponding to the $2p_{3/2}$ and $2p_{1/2}$ orbitals, respectively. AAZ-3 displays similar peaks at slightly lower binding energies of 1022.10 eV ($2p_{3/2}$) and 1045.20 eV ($2p_{1/2}$). The In 3d spectra of ZIS and AAZ-3 in Figure 3b show a doublet with the binding energy separation of 7.54 eV. This splitting is attributed to spin-orbit coupling, implying the In^{+3} peaks at 445.27 eV ($3d_{5/2}$) and 452.81 eV ($3d_{3/2}$) for ZIS. The same doublet for AAZ-3, was deconvoluted to $3d_{5/2}$ and $3d_{3/2}$ associated at 445.14 and 452.68 eV binding energies, respectively. A similar trend was observed in the S 2p fitting shown in Figure 3c. The S 2p HR-XPS spectra consist of two tightly packed peaks for $2p_{3/2}$ and $2p_{1/2}$ at 161.98 and 163.18 eV for ZIS and 161.86 eV and 163.07 eV for AAZ-3. Figure 3d–f presents the HR-XPS spectra of Ag 3d, W 4f, and O 1s for AWO@Ag and AAZ-3.[52] The fitted Ag 3d spectra show a doublet with peaks at 367.89 eV ($3d_{5/2}$) and 373.87 eV ($3d_{3/2}$) for AWO@Ag. The binding energies for the same doublet in AAZ-3 were shifted to 368.01 eV and 373.99 eV, respectively. Metallic Ag was further confirmed from the Ag 3d spectrum, where the doublets associated with Ag^0 were found to be 13.19% in AWO@Ag and 13.12% in AAZ-3. This small deviation is attributed to the comparatively lower amounts of AWO@Ag in AAZ-3 and the shielding effect of ZIS in the ternary composite. For W 4f, significant shifts in binding energies were observed: from 34.64 eV to 34.91 eV for $4f_{7/2}$ and from 36.72 eV to 36.99 eV for $4f_{5/2}$. The O 1s spectra followed similar trend, with lattice oxygen observed at lower binding energies than the oxygen vacancy and chemisorbed oxygen peaks. The lattice oxygen peaks appeared at 530.09 eV for AWO@Ag and 532.08 eV for AAZ-3. While the oxygen vacancies were observed at 530.78 eV and 532.79 eV, and chemisorbed oxygen was identified at 531.85 eV and 533.86 eV in AWO@Ag and ternary composites, respectively. In summary, XPS analysis revealed a red shift in the binding energies for ZIS constituents (Zn, In, and S), and a blue shift associated with AWO constituents (Ag, W, and O) within AAZ-3. The reciprocal shifts in binding energies for ZIS and AWO components suggest the formation of an intimate interface and subsequent interfacial electron transfer between two semiconductors,[53] confirming the formation of a Z-scheme heterojunction between ZIS and AWO@Ag.

To further unveil the interface formation, collaborative morphological studies were conducted using FE-SEM and TEM analysis as follows. Morphological information for AWO@Ag and AWO@Ag/ZIS was collected from FE-SEM and CS-corrected TEM images. **Figure 4a,b** reveals distinct morphologies for ZIS and AAZ-3, leaving no room for ambiguity. The FE-SEM image (Figure 4a) clearly shows the presence of petal-like nanosheet morphology of ZIS, while Figure 4b illustrates the formation of a metallic Ag particulate shell around the hexagonal-shaped rods of AWO, along with ZIS nanosheets over the surface of AWO@Ag. The observed interface between the AWO core and Ag shell indicates favorable surface energy conditions which were created during the hydrothermal synthesis. The encapsulation of AWO microrods underscores the optimized synthesis conditions and highlights the role of Ag in promoting strong adhesion and minimizing interfacial energy. ZIS nanosheets, anchored on the surface of AWO@Ag (Figure 4b), depict the multi-level interface architecture involving a hexagonal core, a particulate shell, and nanosheets wrapped over the core–shell.

TEM analysis provided further insights about ultra-thin nanosheets of ZIS evident from high-resolution imaging (Figure 4c).[54] Dark-field TEM images of AAZ-3 visualize the Ag particles shelled on AWO surface and their collective (AWO@Ag) interaction with ZIS (Figure 4d). The distribution of metallic Ag nanoparticles and their quantified particle size is shown in the inset of Figure 4e. The majority size of Ag particles in shell is found to be 20–30 nm, as determined from the Ag particle size distribution curve, indicating that the LSPR facilitated by the shell formation resonates across blue to red regions of the solar spectrum. Polydispersity in Ag particle size (10-50 nm) contributes to the broad LSPR peak observed in the UV-vis absorbance spectra of AWO@Ag.

The significant ZIS content (87.5%) in AAZ-3 facilitates the wrapping of ZIS around AWO@Ag, resulting in a strong interfacial interaction. Enhanced contrast dark-field imaging and EDX mappings confirm the presence of Ag NPs on the surface of AWO, generating an LSPR effect.[55,56] The dark flake-like nanostructures (Figure 4f) wrapped around AWO@Ag, with stark contrast morphology, represent ZIS nanosheets. Micrographs

© 2025 Wiley-VCH GmbH

16136829, 2025, 34, Downloaded from https://onlinelibrary.wiley.com/doi/10.1002/smll.202501833 by Jeonbuk National University, Wiley Online Library on [18/10/2026]. See the Terms and Conditions (https://onlinelibrary.wiley.com/terms-and-conditions) on Wiley Online Library for rules of use; OA articles are governed by the applicable Creative Commons License

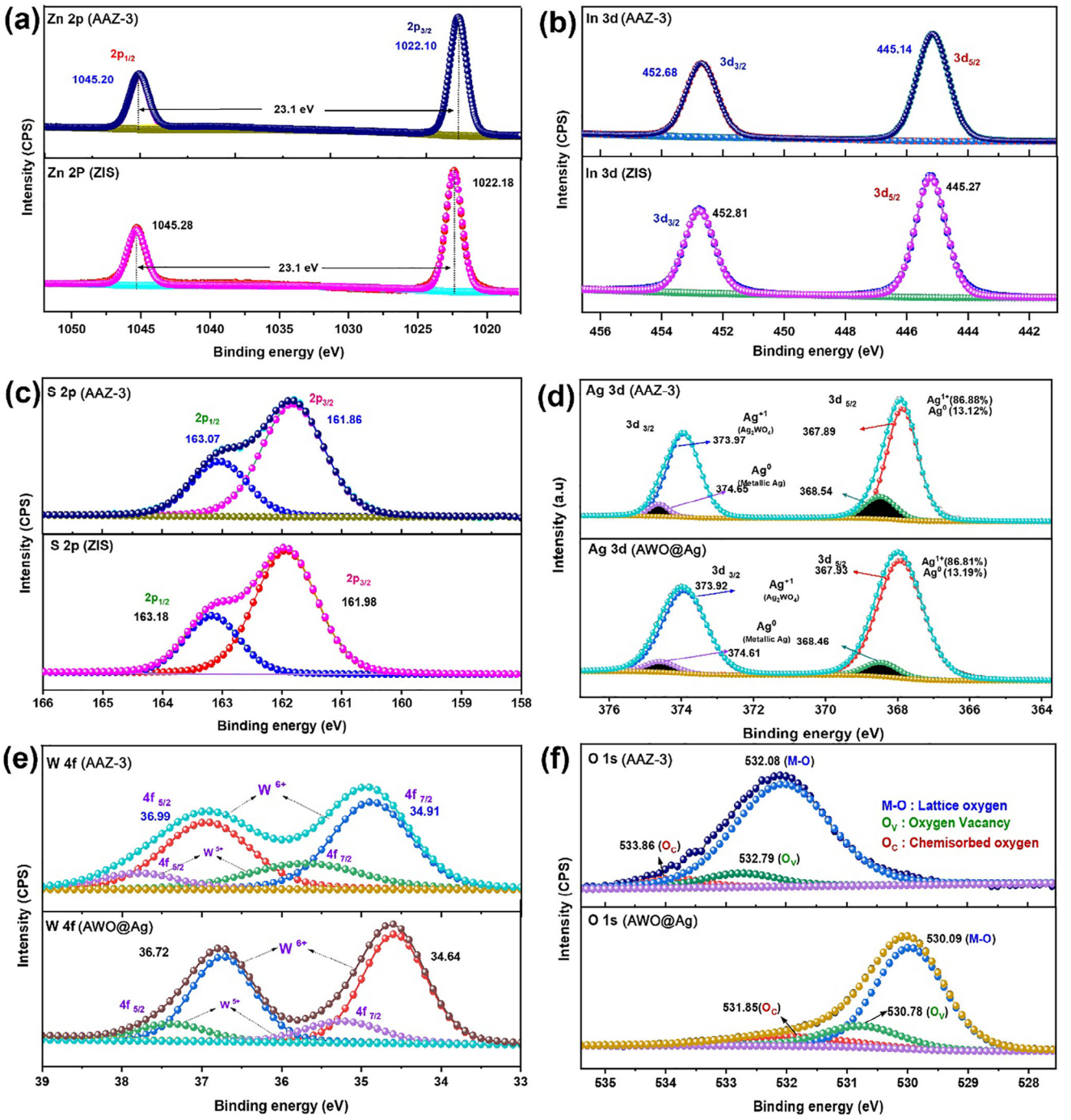


Figure 3. HR-XPS spectra of ZIS, AWO@Ag and AZ-3, a–c) Zn 2p, In 3d, S 2p of AAZ-3 and ZIS; d–f) Ag 3d (Metallic Ag^0 and Ag^{+1}), W 4f, O 1s of AAZ-3 and AWO@Ag.

and mappings of pristine AWO@Ag, ZIS, and AAZ-3 acquired from FE-SEM analysis were presented in Figures S6–S8 (Supporting Information), respectively, further supporting the incorporation of AWO@Ag onto the surface of ZIS. While these morphological observations establish the composite architecture, atomic-level confirmation of the components involved and interface formation across Z-scheme heterojunction components required detailed crystallographic analysis. High-resolution transmission electron microscopy coupled with Fast Fourier Transform (FFT) analysis provided conclusive evidence for the heterojunction architecture of AAZ-3. Two representative regions were examined (Figures S9, S10, Supporting Information), with corresponding FFT patterns revealing distinct lattice fringes from all three constituent components. The FFT diffraction spot analyses (Tables S1 and S2, Supporting Information) quantitatively identified characteristic d-spacings, which were systematically

© 2025 Wiley-VCH GmbH

16136829, 2025, 34, Downloaded from https://onlinelibrary.wiley.com/doi/10.1002/smll.202501833 by Jeonbuk National University, Wiley Online Library on [18/10/2026]. See the Terms and Conditions (https://onlinelibrary.wiley.com/terms-and-conditions) on Wiley Online Library for rules of use; OA articles are governed by the applicable Creative Commons License

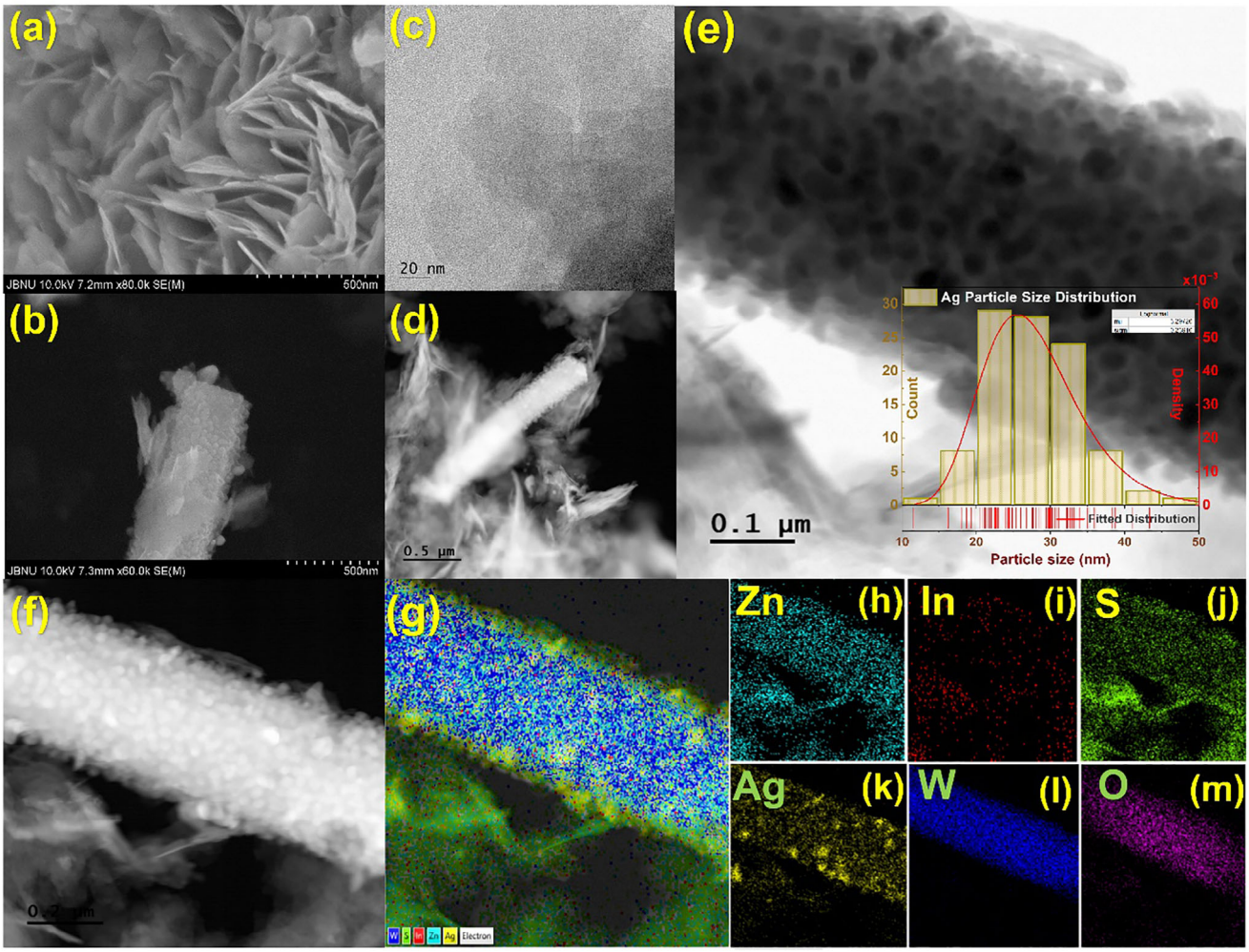


Figure 4. Morphology affirmations a) FE-SEM image of ZIS Petal-like sheets, b) FE-SEM image of AAZ-3 with clear depiction of AWO rod shelled by Metallic Ag NPs and ZIS petals over it, c) HR-TEM micrograph of ultrathin ZIS sheets, d) STEM image of Ag NPs shelled AWO rod, surrounded by ZIS sheets.e) TEM micrograph of AWO@Ag incorporated on ZIS, distribution curve and metallic Ag average particle size (inset) f) Dark field STEM-HAADF image of interface region between AWO@Ag, ZIS in AAZ-3, source image for Elemental mapping; g)EDX sum spectra mapping of AAZ-3; Individual mappings Zn h), In i), S j), Ag k), W l) and O m).

assigned to specific crystallographic planes of each component (Table S3, Supporting Information). Ag_2WO_4 was identified through multiple characteristic d-spacings matching the orthorhombic structure (PDF#70-1719), including (220), (031), (311), and (131) planes with observed d-values ranging from 0.317 to 0.405 nm. The hexagonal $ZnIn_2S_4$ phase (PDF#72-0773) exhibited characteristic (102), (0012), and (111) reflections with d-spacings between 0.204 and 0.323 nm. Additionally, metallic Ag nanoparticles were confirmed through (111) and (200) planes with d-values of 0.232 and 0.201 nm, respectively. Notably, the observed d-spacings exhibited excellent agreement with reference values (XRD), with deviations consistently below 0.006 nm (Table S4, Supporting Information). This strong correlation between HRTEM and XRD measurements validates the crystallographic integrity of the heterojunction. The atomic-level confirmation of AWO planes (6), ZIS planes (4), and metallic Ag planes (2) demonstrate successful composite formation. Critically, HRTEM results demonstrate intimate interfacial contact among the AWO@Ag and ZIS, providing direct microscopic evidence for the efficient charge transfer pathways characteristic of the Z-scheme heterojunction.

Using STEM micrograph as a source for EDX analysis, elemental mappings were acquired. Figure 4g, depicts the mappings of all the elements present in AAZ-3, induvial mappings for Zn, In, S, Ag, W, and O and are depicted in Figure 4h–m, respectively. With the map sum spectrum shown in Figure S11 (Supporting Information).

2.1. Photocatalytic Hydrogen Production Performance

The photocatalytic activities of the prepared specimens, including AAZ-3, pristine AWO@Ag, ZIS, and other binary and ternary nanocomposite photocatalysts, were systematically evaluated through H_2 generation tests after their structural and morphological characterization.

© 2025 Wiley-VCH GmbH

16136829, 2025, 34, Downloaded from https://onlinelibrary.wiley.com/doi/10.1002/smll.202501833 by Jeonbuk National University, Wiley Online Library on [18/10/2026]. See the Terms and Conditions (https://onlinelibrary.wiley.com/terms-and-conditions) on Wiley Online Library for rules of use; OA articles are governed by the applicable Creative Commons License

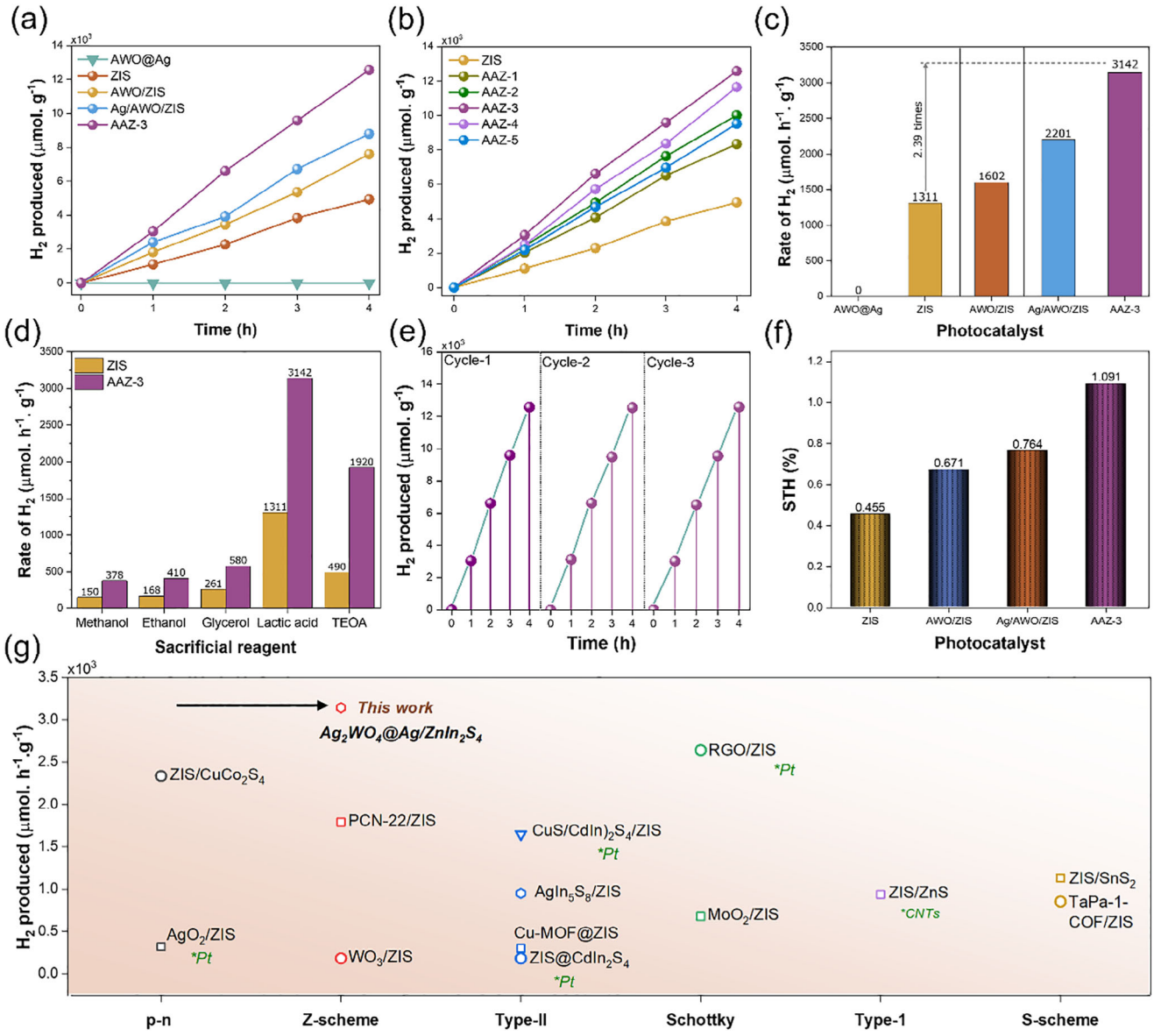


Figure 5. Photocatalytic H_2 production a) Amount H_2 produced by AWO@Ag, ZIS, AWO/ZIS, Ag/AWO/ZIS and AWO@Ag/ZIS b) AAZ-1,2,3,4 & 5 H_2 generation performance in 1 cycle (4 h) c) Rate of H_2 generated by pristine, binary and ternary composites d) Study on effect of sacrificial reagent on photocatalytic performance of ZIS and AAZ-3. e) recyclability studies of AAZ-3, f) STH evaluation for H_2 generation capable photocatalysts. g) Recently reported literature in connection to the photocatalytic H_2 production using $ZnIn_2S_4$ based systems.

The photocatalytic H_2 generation rates of the as-synthesized composite materials were assessed to identify an optimized photocatalyst with robust redox capabilities. As expected, pristine AWO, Ag/AWO, and AWO@Ag exhibited negligible H_2 evolution due to insufficient potential for proton reduction to generate molecular H_2.[57] Even when using sacrificial reagents such as glycerol, methanol, and TEOA, these photocatalysts showed no traceable H_2 generation activity. Subsequently, pristine ZIS and a series of Ag-shelled AWO over ZIS (AWO@Ag/ZIS) photocatalysts, named AAZ-1, AAZ-2, AAZ-3, AAZ-4, and AAZ-5, were tested for photocatalytic hydrogen production and compared with the performances of AWO@Ag, ZIS, AWO/ZIS, Ag-loaded AWO/ZIS. All photocatalysts were tested for one cycle lasting ≈4 h, with the results presented in **Figure 5**a,b.

The results demonstrated that the AAZ-3 (AWO@Ag/ZIS) photocatalyst exhibits the highest activity compared to ZIS, AWO/ZIS, and Ag/AWO/ZIS (Figure 5a). This increment in H_2 rates conveys the importance of incessant charge transfer facilitated by Ag-shell structure, which improves charge separation dynamics. Further improved results toward photocatalytic H_2 production were observed for the series of AWO@Ag loaded ZIS nanosheets photocatalysts with varying weight percentages, and the activity rates are shown in Figure 5b. AAZ-3 showed the maximum H_2 accumulation of 12.568 μmol h^{-1}. $g^{-1}_{cat.}$ after 4 h. Figure 5c shows the rate of H_2 evolution for the as-synthesized

© 2025 Wiley-VCH GmbH

16136829, 2025, 34, Downloaded from https://onlinelibrary.wiley.com/doi/10.1002/smll.202501833 by Jeonbuk National University, Wiley Online Library on [18/10/2026]. See the Terms and Conditions (https://onlinelibrary.wiley.com/terms-and-conditions) on Wiley Online Library for rules of use; OA articles are governed by the applicable Creative Commons License

materials. Pristine ZIS exhibited the lowest activity with the H_2 rates of 1311 μmol h^{-1}. $g^{-1}_{cat.}$, among all the tested catalysts capable of H_2 production. AWO/ZIS has shown a slightly improved H_2 production performance with 1602 μmol h^{-1}. $g^{-1}_{cat.}$, although AWO is not a visible active semiconductor to generate photo-holes and photo-electrons. This enhancement in activity of AWO/ZIS could be attributed to the charge trapping centers facilitated by AWO or the attained structural stability of ZIS with AWO addition. Ag-loaded AWO combined with ZIS (Ag/AWO/ZIS) also exhibited enhanced photocatalytic performance, achieving H_2 production rate of 2201 μmol h^{-1}. $g^{-1}_{cat.}$, which is attributed to the co-catalytic behavior of Ag particles as electron sink and enhanced exciton lifetime.

The highest H_2 accumulation was observed for AAZ-3, consisting of Ag NPs shelled over a hexagonal rod-shaped AWO core, further modified with ultrathin ZIS nanosheets (AWO@Ag/ZIS). AAZ-3 demonstrated a splendid H_2 production performance of 3142 μmol h^{-1}. g^{-1}_{cat}, which is 2.39 times higher than that of pristine ZIS. To get a better understanding of the role of sacrificial reagents, ZIS and AAZ-3 were tested with diverse hole scavengers, as shown in Figure 5d. Among the tested reagents, TEOA and lactic acid yielded the most favorable H_2 production rates compared to other alcohols.

Additionally, the recyclability of AAZ-3 was tested over three consecutive cycles (12 h) to study its long-term stability, with the results presented in Figure 5e. For each reaction cycle, the solution was degassed and purged with ultra-high-purity nitrogen every 4 h. The results delineate that the photocatalyst remains highly stable across multiple H_2 production cycles.[58] Extended stability evaluation beyond the three cycles depicted in Figure 5e revealed noteworthy performance characteristics. Continuous hydrogen evolution measurements spanning 40 h (Figure S12, Supporting Information) demonstrated robust catalytic stability for seven consecutive cycles, with hydrogen yield of 130 mmol g^{-1} after 28 hours of testing. Subsequently, a progressive activity decline occurred between cycles 7–10. This stability pattern suggests gradual surface modifications rather than bulk structural deterioration, likely attributable to progressive active site deactivation or shielding or interfacial passivation. Correlation with post-reaction characterization data (XPS, XRD, FTIR) discussed in later sections, which confirmed the preservation of crystallographic and chemical architecture, substantiates this hypothesis. The observed deactivation kinetics, characterized by gradual rather than abrupt decline, implies that the implementation of regeneration protocols or refined operational parameters could potentially mitigate performance loss. These comprehensive stability assessments establish that the AAZ-3 heterojunction maintains catalytic stability in the long run, substantially beyond the preliminary cycles, while indicating that maintenance procedures would help sustain optimal performance over extended periods.

The solar-to-hydrogen (H_2) efficiency for the half-reaction using lactic acid as a sacrificial electron donor was calculated under simulated solar irradiation. The parent, binary, ternary, and champion photocatalysts was also evaluated as shown in Figure 5f. AAZ-3 shows the highest STH efficiency of 1.091%, whereas pristine ZIS shows only 0.45% toward STH efficiency. The order of STH efficiency among the prepared photocatalysts was AAZ-3(AWO@Ag/ZIS) > Ag/AWO/ZIS > AWO/ZIS > ZIS.

To further evaluate the potential of this novel combination, AQY was estimated using a standard formula, and a comparative study of AAZ-3 with ZIS-based heterostructures for photocatalytic H_2 production based on the calculated AQY at 400 nm, was conducted based on recent reports as shown in Figure 5g (details provided in Table S7, Supporting Information).

2.2. Photocatalytic Dye Degradation Performance

The photocatalytic dye degradation performance of the as-synthesized photocatalysts was evaluated against 20 ppm of methyl orange (MO) under visible light irradiation. **Figure 6a–f** summarizes the results of the MO degradation experiments. As shown in Figure 6a, photolysis of blank MO was performed under visible light irradiation for 1 h, resulting in negligible degradation. Thereafter, the photocatalytic MO degradation efficiencies for all the as-synthesized photocatalysts were tested under the same conditions. Pristine AWO@Ag showed the least degradation efficiency due to the band structure of AWO, which failed to directly generate superoxide radicals essential for the degradation process. In contrast, the pristine ZIS succeeded in degrading more than 60% of the dye within 1 h, as it can efficiently liberate superoxide species. A slight improvement was observed for AWO/ZIS photocatalyst, but the large bandgap of AWO restricted the light absorption to wavelengths below 400 nm, which could not generate photoelectrons and holes in the visible spectrum, thereby limiting the efficiency. Ag-loaded AWO/ZIS photocatalyst exhibited better efficiency than AWO/ZIS, but the degradation outcome is comparatively inferior to that of Ag-shelled composites. The best improvement was observed for Ag-shelled AWO over ZIS photocatalysts.

Figure 6b shows the natural logarithms of C/Co (corresponds to C/Co values of Figure 6a) and their fitted values, representing the pseudo-first-order kinetics of the degradation process. Figure 6c presents the UV–vis absorbance spectra of aliquots collected during MO degradation using AAZ-3 at different time intervals ranging from 0 to 60 min. Figure 6d shows the C/Co values for a series of AAZ photocatalysts in comparison to pristine ZIS and AWO@Ag. The results indicate that AAZ-3 (ZIS loaded with 12.5 wt% AWO@Ag) shows exceptionally high redox reaction feasibility, attaining a degradation rate of 97.16%. However, with further increase in AWO@Ag content (>12.5%), the degradation performance decreases, which is likely due to the shielding effect of the AWO@Ag around the ZIS semiconductor, which covers the active sites of ZIS and exceeds the internal charge carrier recombination at the Z-scheme interface. Consequently, the MO degradation efficiency of the catalysts followed the order: AAZ-3 > AAZ-4 > AAZ-2 > AAZ-5 > AAZ-1 > ZIS > AWO@Ag. Photographs of aliquots collected at different intervals, demonstrating the color changes over 1 h, are presented in Figure S13 (Supporting Information).

Natural logarithmic fittings for AAZ photocatalysts series was presented in Figure 6e. The fitting data revealed a straight line from an origin, which depicts the pseudo-first-order rate kinetics of the manifested photodegradation system,[34] so that the degradation efficiency of the system was directly proportional to the rate constant. The rate constant values of all the specimens were depicted in Figure 6f. AAZ-3 exhibited the highest rate

© 2025 Wiley-VCH GmbH

16136829, 2025, 34, Downloaded from https://onlinelibrary.wiley.com/doi/10.1002/smll.202501833 by Jeonbuk National University, Wiley Online Library on [18/10/2026]. See the Terms and Conditions (https://onlinelibrary.wiley.com/terms-and-conditions) on Wiley Online Library for rules of use; OA articles are governed by the applicable Creative Commons License

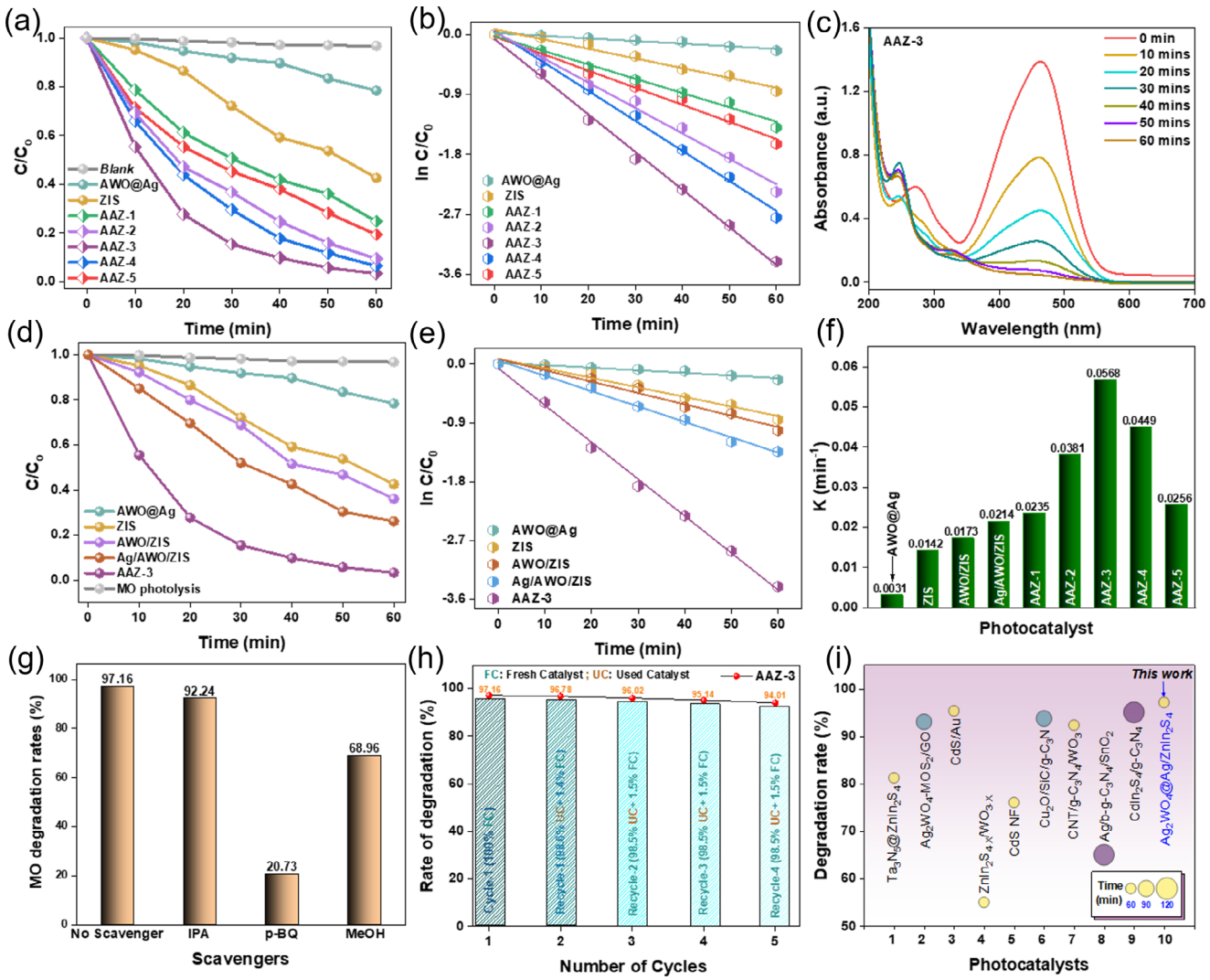


Figure 6. Methyl Orange (MO) Photocatalytic dye degradation-controlled experiments and recyclability studies a) C/Co Values of Blank MO photolysis, AWO, ZIS, AWO/ZIS, Ag/AWO/ZIS and AAZ-3. b) Natural log values of C/Co collected from Figure 6(a). c) UV–vis's absorption spectra of MO dye degraded using AAZ-3 at different time intervals (0-60 min). d,e) C/Co Values of Blank MO photolysis, AWO@Ag, ZIS, AAZ-1,2,3,4 and 5 and corresponding Natural log values of C/Co respectively f) Rate constant derived from the slope of natural Logs of C/Co. g) Radical scavenging tests, h) recyclability of AAZ-3 and i) Literature survey for comparative study with the present work.

constant value of 0.0568 min^{-1}, which is 18.93 times higher than that of pristine AWO@Ag (0.0031 min^{-1}) and 4.05 times higher than ZIS (0.0142 min^{-1}). The enhanced photocatalytic activity of AAZ-3 is attributed to its prolonged charge carrier lifetime and the formation of an Ag-mediated Z-scheme heterojunction at the AWO/ZIS interface. Tailoring the interface based on band structures of the individual component further optimized its performance. The rate constant value of all the specimens along with their efficiencies is tabulated in Table S6 (Supporting Information).

Radical trapping experiments were conducted to understand the generation and utilization of reactive radicals during MO photodegradation. The experiments were performed under constant conditions with 1 mmol L^{-1} scavengers added to the reaction mixture. p-Benzoquinone (p-BQ), methanol (MeOH), and isopropyl alcohol (IPA) were used as trapping agents for superoxide radicals ($\bullet O_2^-$), photo-holes (h^+), and hydroxyl radicals ($\bullet OH$), respectively.[59] As depicted in Figure 6g, AAZ-3 exhibited a degradation efficiency of 97.16% in the absence of scavengers. However, with the addition of MeOH, the efficiency decreased to 68.96%; with p-BQ, it dropped significantly to 20.73%. In contrast, the addition of IPA results in a minimal decrease to 92.24%, as shown in Figure 6h. The observed minimal IPA effect over AAZ-3 can be attributed to the action of AWO@Ag, as IPA cannot significantly affect the ZIS degradation ability due to its weak oxidation potential associated valence band (+1.65 eV).[60] Comparatively, a substantial drop-in activity toward $\bullet O_2^-$ radicals and photoholes was observed, which could be produced by both AWO@Ag (indirectly from hydroxy radicals) and ZIS (directly). From these findings, it is noticeable that the incorporation of Ag NPs on AWO rods with their inherent LSPR properties potentially enhances the photocatalytic efficacy of the system in two distinct

© 2025 Wiley-VCH GmbH

16136829, 2025, 34, Downloaded from https://onlinelibrary.wiley.com/doi/10.1002/smll.202501833 by Jeonbuk National University, Wiley Online Library on [18/10/2026]. See the Terms and Conditions (https://onlinelibrary.wiley.com/terms-and-conditions) on Wiley Online Library for rules of use; OA articles are governed by the applicable Creative Commons License

ways. First, the LSPR helps the AWO to rapidly excite conduction electrons by enabling it to absorb and shuttle photon energy. This energy can be thereby transferred to neighboring ZIS particles through a process known as plasmon-induced resonance energy transfer (PIRET).[61] The transferred energy promotes the generation of electron–hole pairs within the ZIS, which is crucial for driving photocatalytic reactions. Second, the valence band maximum (VB_{max}) of AWO can directly generate powerful hydroxyl (•OH) radicals via a hot electron mechanism in visible light, which can be further converted to superoxide radicals. These photogenerated •OH radicals play a significant role in dye degradation due to their strong oxidation capability. Further to confirm the individual reduction capabilities of AWO@Ag and ZIS and their collective performance in optimal loadings (AAZ-3), a nitro blue tetrazolium (NBT) test has been conducted to trace the superoxide radicals generated under 30 mins of light irradiation. The NBT test was used as a detecting agent for superoxide species which further confirmed the charge transfer mechanism. NBT analysis provided direct chemical evidence for superoxide radical ($\bullet O_2^-$) generation in each single test, the obtained absorption spectra for all the specimens are given in Figure S14 (Supporting Information). The NBT reduction assay, monitored through characteristic absorption changes at ≈260 nm, revealed distinct behaviors among the tested materials. After illumination, pristine ZIS and AWO@Ag exhibited modest absorption decreases of 53% and 22.5% respectively, indicating limited $\bullet O_2^-$ production capacity as individual components. AWO@Ag exhibited positive result in NBT test is attributable to the localized surface plasmon resonance (LSPR) effect of metallic Ag nanoparticles rather than semiconductor photocatalysis, as evidenced by its negligible hydrogen evolution activity. Strikingly, the AAZ-3 heterojunction demonstrated pronounced NBT reduction under identical conditions, manifesting as a dramatic 91.4% decrease in absorption intensity. This enhanced superoxide generation directly corroborates the efficient charge separation in the Z-scheme architecture, where photogenerated electrons accumulate at the ZIS conduction band with sufficient reductive potential for O_2 reduction. Crucially, the dark control experiment showed negligible NBT transformation, confirming the light-dependent nature of radical formation. The hierarchical $\bullet O_2^-$ production (AAZ-3 >> ZIS >> AWO@Ag) supports our proposed Z-scheme mechanism, where electrons from AWO@Ag recombine with holes from ZIS, preserving the most reductive electrons for oxygen activation. These results provide complementary validation to our radical trapping experiments and establish the superior reactive oxygen species generation capability of the engineered heterojunction.

The recyclability test of AAZ-3 was further assessed to evaluate its stability and durability. Unlike conventional recyclability studies, a consistent catalyst loading of 1 g L^{-1} was maintained throughout five cycles. After each degradation test, the catalyst was allowed to settle, and the supernatant was carefully removed. Settling time was monitored, and complete settling occurred within 1 h, leaving a clear supernatant (Figure S15, Supporting Information). The recovered catalyst was washed, dried at 100 °C for 6 h, and a small amount of fresh AAZ-3 was added to maintain a 1 g L^{-1} loading. Figure 6h illustrates the results, showing a slight decrease in efficiency (3.15%) after four cycles. Despite this, the overall performance remained stable, demonstrating the versatile chemical and mechanistic stability of AAZ-3 in photocatalytic applications. A comparative study of MO degradation performance among ZIS-based photocatalysts is shown in Figure 6i. The present work achieved a superior degradation efficiency of 97.16% for 20 ppm MO dye within 60 min, outperforming other ZIS-based systems reported in the literature (Table S9, Supporting Information).

2.3. Photoelectrochemical (PEC) Water Splitting Performance

The potential of the fabricated photoelectrodes for photoelectrochemical water splitting was elucidated through PEC analysis. Cyclic voltammetry (CV) performance was initially investigated at scan rate of 50 mV s^{-1}. As shown in Figure S16 (Supporting Information), the CV curves of AWO@Ag and ZIS photocatalysts showed moderate photocathodic currents of 0.6 and −2.7 mA cm^{-2} at 0.4 V versus RHE, respectively, and photoanodic currents of 0.9 and 0.21 mA cm^{-2} at 2.2 V versus RHE, respectively. These results reveal reasonable potential for hydrogen evolution reaction (HER) and oxygen evolution reaction (OER) performances. In contrast, the CV curve of optimized binary composite (AAZ-3) exhibited significantly higher current densities in diverse directions at the same potentials: 4.37 mA cm^{-2} (photocathode) at 0.4 V and 5.62 mA cm^{-2} at 2.2 V (photoanode) versus RHE. This confirms the enhanced bifunctionality behavior (HER and OER) of AAZ-3 over its pristine counterpart.

It is noteworthy that the development of photoanodes has garnered more attention than photocathodes due to the challenges associated with OER process, such as the 4-electron process and the comparatively higher overpotential of 1.23 V required for water oxidation.[62,63] Accordingly, a series of Ag-shelled AWO as-synthesized on ZIS photocatalysts were rationally designed to possess strong redox activity and investigated for OER applications.

The PEC- OER capabilities of pristine, binary, and ternary photoelectrodes (photoanodes) were assessed under visible light irradiation (380–800 nm) by examining their solar-to-fuel conversion efficiency toward photoelectrochemical water splitting reaction. **Figure** 7a,b presents the anodic currents for all the as-synthesized photoelectrodes. As shown in Figure 7a, ZIS and AWO@Ag showed the lowest current density, followed by AWO/ZIS, which can be attributed to the swift recombination of photogenerated charge carriers. The highest photocurrent enhancement was observed with AAZ-3, this indicates that the shell structure formed by Ag significantly reduced the intrinsic electron–hole recombination of ZIS.[64] AAZ-3 demonstrated impressive photocurrents of 3.91 mA cm^{-2}, which is 12.01 times higher than pristine ZIS (0.325 mA cm^{-2}) and 7.51 times than pristine AWO@Ag (0.519 mA cm^{-2}) at 2.2 V versus RHE. This enhancement aligns with the establishment of proper band positions in the junction photoanode for PEC water oxidation reactions.

Figure 7b depicts the photo-induced current densities of all Ag-shelled composites (AAZ-1, AAZ-2, AAZ-3, AAZ-4 and AAZ-5). The anodic photocurrents of AAZ-1, AAZ-2, AAZ-3, AAZ-4, and AAZ-5 are 0.4, 0.78, 3.91, 1.78, and 1.13 mA cm^{-2} at 2.2 V versus RHE, respectively. Thereafter, open-circuit potential (OCP) measurements were conducted to determine the extent of photogenerated charge carriers accumulated in the material. A cathodic (negative) shift in the voltage magnitude under light irradiation

© 2025 Wiley-VCH GmbH

16136829, 2025, 34, Downloaded from https://onlinelibrary.wiley.com/doi/10.1002/smll.202501833 by Jeonbuk National University, Wiley Online Library on [18/10/2026]. See the Terms and Conditions (https://onlinelibrary.wiley.com/terms-and-conditions) on Wiley Online Library for rules of use; OA articles are governed by the applicable Creative Commons License

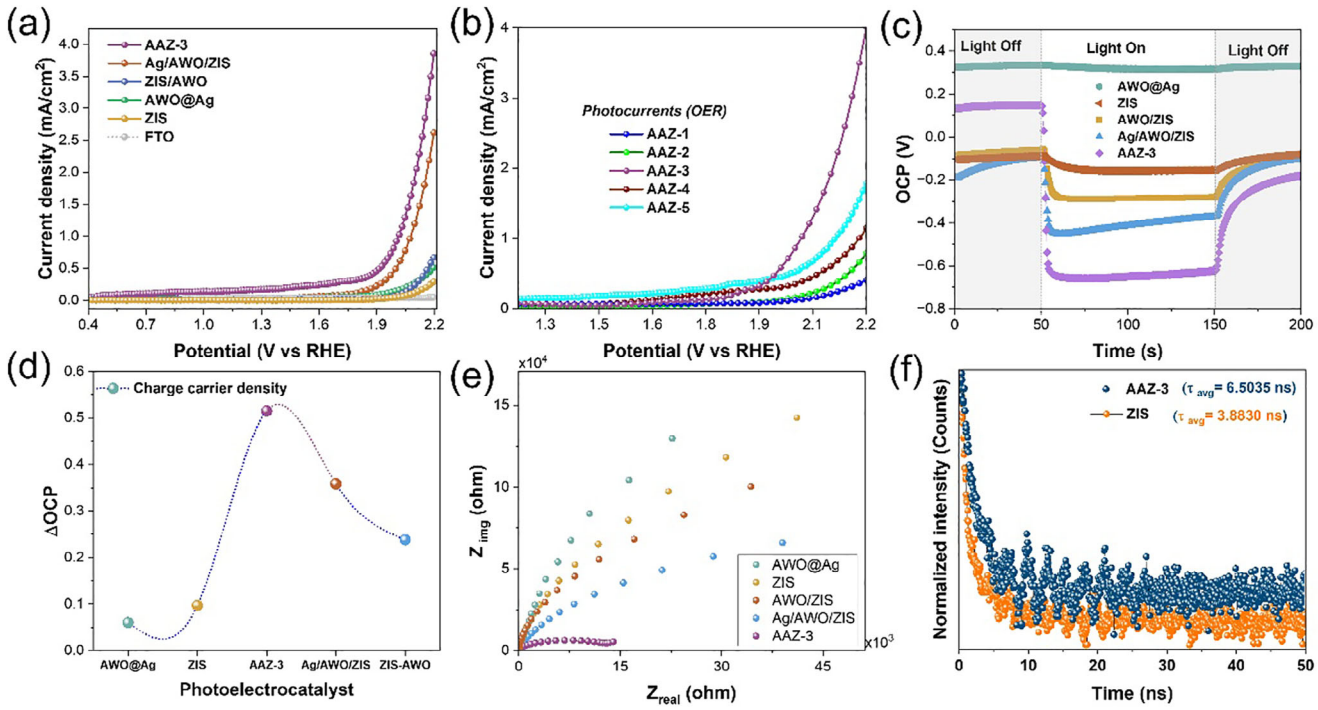


Figure 7. Photoelectrochemical analysis a,b) Photoelectrochemical water oxidation performance (OER) of neat FTO, AWO@Ag, ZIS, AWO/ZIS, Ag/AWO/ZIS and AWO@Ag/ZIS. OER activities of AAZ-1,2,3,4 and 5. c,d) OCP analysis and respective charge carrier density measurements, e) Impedance spectra of pristine, binary and ternary composites f) TRPL analysis of ZIS and champion ternary composite AAZ-3.

depicts the degree of electron accumulation at the working electrode surface, with greater negative shifts implying higher separation efficiency of the photogenerated charge carriers. Comparative analysis with existing ZIS-based photoelectrochemical systems reveals distinctive performance characteristics of our AAZ-3 photoanode (Table S8, Supporting Information). AAZ-3 stands out among all the reports with the highest current densities of 3.91 mA cm^{-2}. However, this enhanced current generation occurs at an operating potential of 2.2 V versus RHE, which exceeds typical overpotential values for PEC water splitting. This elevated voltage suggests increased overpotential requirements, contrasting with systems optimized for minimal energy input. The observed performance trade-off of exceptional photocurrent at higher potential reflects the electronic structure inherent to our Z-scheme configuration, which prioritizes charge carrier separation over thermodynamic efficiency. For applications prioritizing maximum hydrogen production over operational energy requirements, this substantial photocurrent enhancement establishes AAZ-3 as a benchmark photoelectrode in $ZnIn_2S_4$-based systems.

Figure 7c presents the OCP measurements of the photoelectrodes conducted at room temperature. AAZ-3 exhibited the highest negative potential shift, depicting the highest accumulation of the photogenerated charge carriers and subsequent separation efficiency in the photoanode material. The differential open circuit potential (ΔOCP) measured from the OCP measurements, has been shown in Figure 7d. AAZ-3 exhibited the highest ΔOCP value of 0.515 V which is nearly five times higher than pristine ZIS. This indicates that AAZ-3 not only produces a higher number of excitons but also utilizes the generated excitons, directly correlating to improved separation efficiency of photogenerated charge carriers. The systematic enhancement in ΔOCP values from pristine materials (ZIS, AWO@Ag) to binary and ternary nanostructures (AWO/ZIS and Ag/AWO/ZIS) and ultimately to the Ag-shelled composite (AAZ-3) underscores the success of the mechanistic design and strategic integration of Ag NPs-shelled AWO with ZIS in forming the Ag_2WO_4@Ag/$ZnIn_2S_4$ interfaced composite. This integration successfully elevates photogenerated charge carrier dynamics, improving PEC-OER results. The observed trend in OCP supports the enhanced redox properties of AAZ-3 for photocatalytic and PEC performances. Thereafter, the applied bias photon-to-current efficiency (ABPE%) was derived from the OER plots for ZIS, AWO@Ag, and AAZ-3. As shown in Figure S17 (Supporting Information), AAZ-3 demonstrates 5 times and 8 times higher photoconversion efficiency as compared to pristine AWO@Ag and ZIS, respectively. Since the charge transfer resistance is an indication of the supply of photoelectrons ability to any material, electrochemical impedance spectroscopy was investigated. The charge transfer resistance dynamics of any material can be understood from their corresponding Warburg resistance. The Nyquist plots obtained from the electrochemical impedance spectra of the as-synthesized samples are presented in Figure 7e. The smaller semicircular arc indicates less charge transfer resistance across the electrode/electrolyte interface. The smallest semicircular arc is observed for AAZ-3 compared to pristine (ZIS, AWO@Ag), binary AWO/ZIS, and Ag-doped AWO/ZIS (Ag/AWO/ZIS). This further corroborates the higher efficiency of the AAZ-3 photoanode for OER applications.

© 2025 Wiley-VCH GmbH

16136829, 2025, 34, Downloaded from https://onlinelibrary.wiley.com/doi/10.1002/smll.202501833 by Jeonbuk National University, Wiley Online Library on [18/10/2026]. See the Terms and Conditions (https://onlinelibrary.wiley.com/terms-and-conditions) on Wiley Online Library for rules of use; OA articles are governed by the applicable Creative Commons License

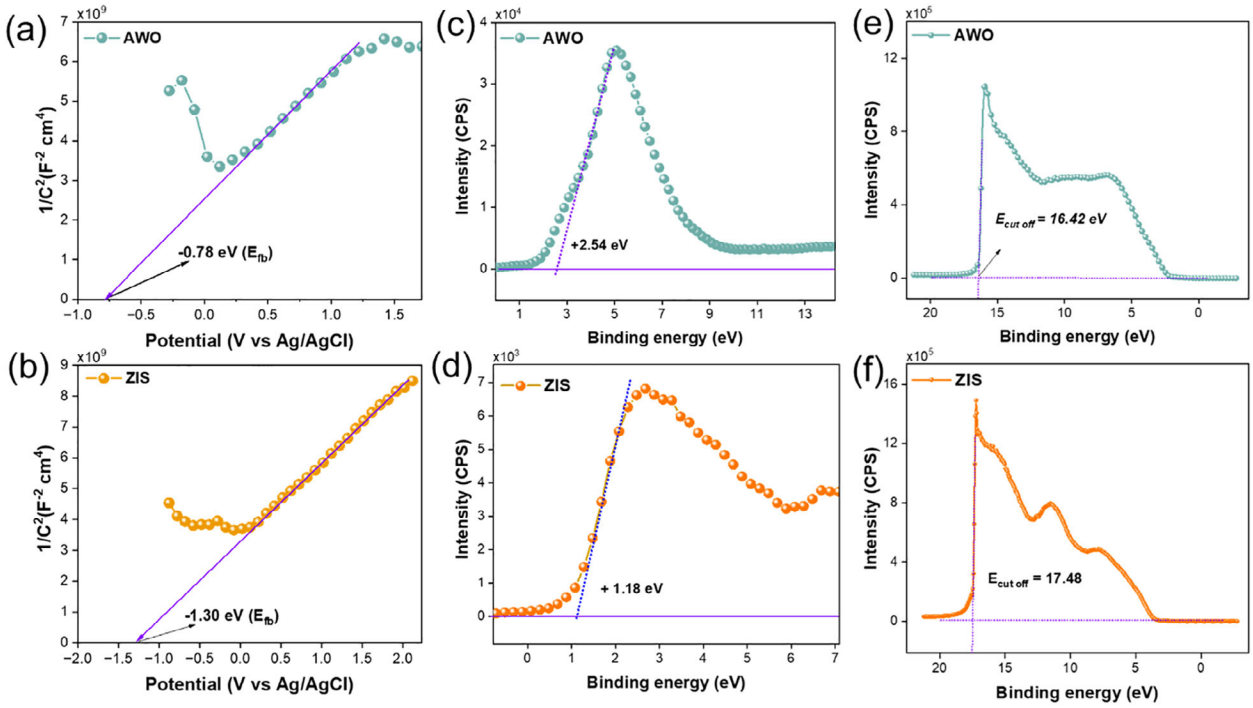


Figure 8. Band structure and Band edge potential analysis a,b) Mott–Schottky plots c,d) VB-XPS spectra e,f) UV photoelectron spectroscopy (UPS) analysis of AWO and ZIS.

The charge transfer efficiency of the photoanodes were investigated from steady-state photoluminescence (PL) and time-resolved PL (TRPL) studies. The steady-state PL spectra of all the AAZ photocatalysts, compared to pristine ZIS, were recorded at an excitation wavelength of 320 nm, as presented in Figure S18 (Supporting Information). A greater quenching in the photoluminescence intensity corresponds to a longer lifetime of photo charge carriers. The emission bands appear at ≈450–550 nm for ZIS, AAZ-1, AAZ-2, AAZ-3, AAZ-4, and AAZ-5 with the absorption band edge of ZIS. The highest quenching was shown in AAZ-3 photocatalyst, which affirms its enhanced charge carrier lifetime for various photocatalytic and photoelectrochemical applications. To gain deeper insight into the lifetime of charge carriers and corroborate the charge transfer process in the synthesized materials, TCSPC (time-correlated single photon counting) assisted analysis was carried out. As shown in Figure 7f, the decay times of ZIS and AAZ-3 was fitted well with a double exponential function.[65] The average lifetime of charge carriers in ZIS is 3.88 ns, whereas AAZ-3 exhibits a much longer lifetime of 6.50 ns. This extension is attributed to the intimate interaction between the AWO core with the metalized Ag particulate shell and the ZIS nanosheets that enhanced charge carrier separation while suppressing radiative recombination, thereby improving PEC as well as photocatalytic performance.

2.4. Analysis of Electronic Band Structure and Heterojunction Feasibility

From the photocatalytic and photoelectrochemical results as well as the charge transfer dynamics and charge carrier lifetime analyses, it is proved that the integration of AWO@Ag strongly suppresses the intrinsic electron–hole recombination of ZIS and increases the efficiency of the system. The formation of a heterojunction between ZIS and AWO@Ag is the primary mechanism responsible for this synergy. To investigate the nature of this heterojunction, the bandgaps and band structures of the pristine materials were examined by using Mott-Schottky (M-S) analysis, ultraviolet photoelectron spectroscopy (UPS), and valence band X-ray photoelectron spectroscopy (VB-XPS).

The conduction band minimum (CB_{min}) positions of ZIS and AWO were estimated from Mott Schottky (M-S) analysis performed at 500 Hz under dark conditions. **Figure** 8a,b presents the flat band potentials of pristine ZIS and AWO, derived from the M-S plots. Both the pristine materials exhibited negative slopes, indicating their n-type electronic nature. The flat band potential of ZIS was determined to be −1.30 V versus Ag/AgCl, which is more negative than that of AWO (−0.78 V versus Ag/AgCl), conveying that ZIS has a stronger reducing ability than AWO. As the pristine materials are n-type, their flat band potentials are positioned ≈0.1 eV lower than their CB_{min}. Based on the flat band potentials, the CB_{min} of ZIS is determined to be −0.78 eV, V versus RHE and that of AWO was −0.27 eV, V versus RHE (calculated using the equation $E(Ag/AgCl) + 0.059 \times pH + E°(Ag/AgCl)$, where $E°(Ag/AgCl)$ is the standard potential of Ag/AgCl reference electrode (0.197 V at 25 °C)).

UPS analysis was carried out to estimate the work functions of AWO and ZIS, determined to be 4.78 and 3.84 eV, respectively, relative to the vacuum (Figure 8e,f). Conversion to the RHE scale using the standard formulae ($-E_{vac} = E_{RHE} + 4.55$ eV) derived the Fermi levels of ZIS at −0.66 eV versus RHE and AWO at +0.28 eV. To estimate the position of the valence band maximum

© 2025 Wiley-VCH GmbH

16136829, 2025, 34, Downloaded from https://onlinelibrary.wiley.com/doi/10.1002/smll.202501833 by Jeonbuk National University, Wiley Online Library on [18/10/2026]. See the Terms and Conditions (https://onlinelibrary.wiley.com/terms-and-conditions) on Wiley Online Library for rules of use; OA articles are governed by the applicable Creative Commons License

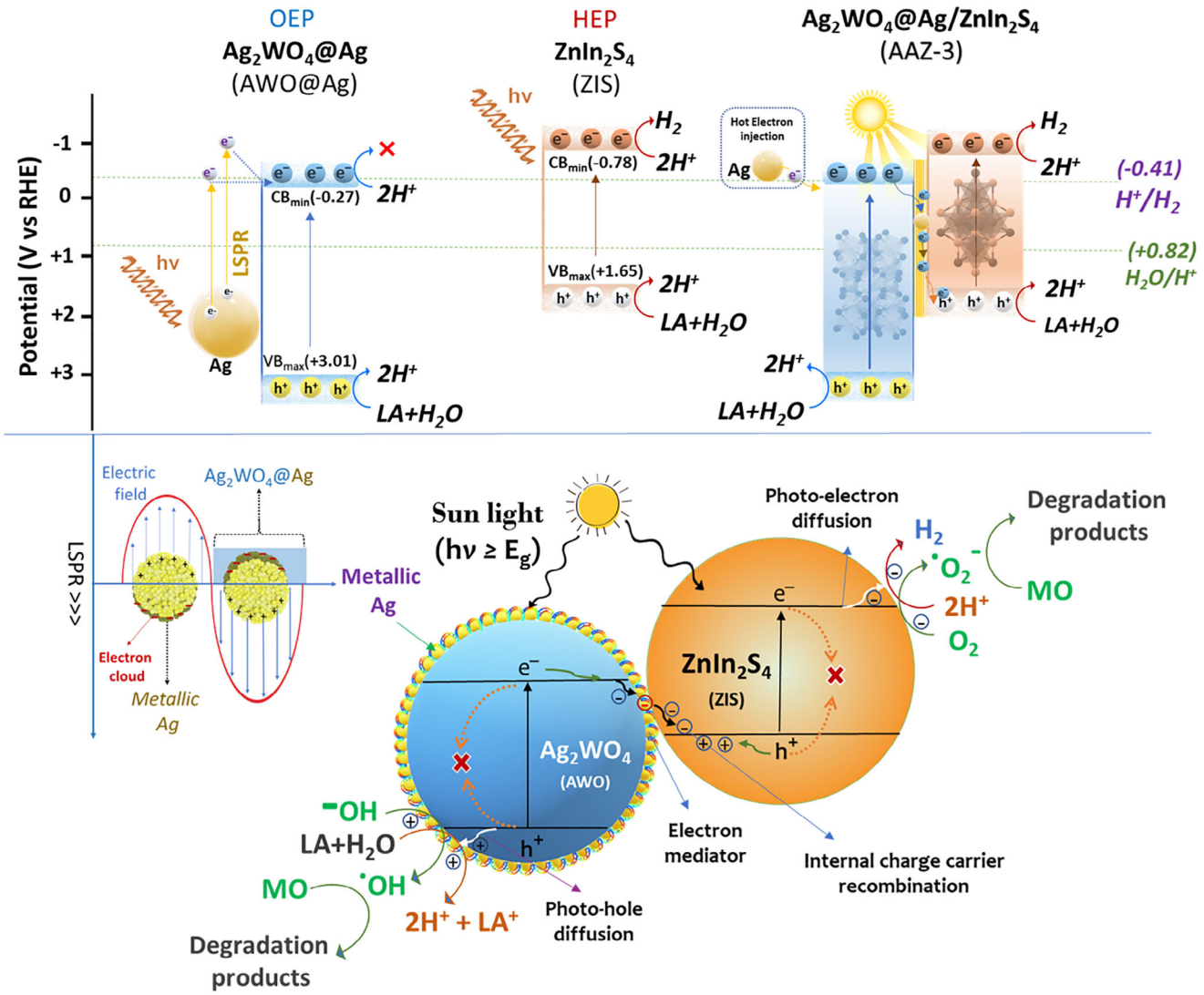


Figure 9. Plausible reaction mechanism a) at AWO b) at ZIS c) At the Z-scheme interface d) Overall charge transfer mechanism involved in AWO@Ag/ZIS for H_2 production and dye degradation.

(VB_{max}), VB-XPS analysis was performed. From the VB-XPS results, VB_{max} was found to be at +1.18 eV for ZIS and +2.54 eV for AWO (Figure 8c,d). The determined VB_{max} values against RHE scale are measured using the equation:[66]

$$E_{VB,RHE} = \Phi + E_{VB,XPS} - 4.44 + 0.0591 \times pH \quad (1)$$

where ϕ is the work function of the instrument. The determined VB_{max} values were determined to be +1.65 eV for ZIS and +3.01 eV for AWO.

Correlating the results from M-S, UPS, and VB-XPS analyses, the plausible charge transfer mechanism for H_2 production and dye degradation in Ag NPs shelled AWO over ZIS (AAZ-3) is depicted in **Figure 9**. The charge transfer dynamics at the interface of the individual components (AWO@Ag, ZIS) are clearly illustrated. The thermodynamic requirements for water splitting reaction and dye degradation were also presented on the RHE scale at neutral pH. For dye degradation, the insufficient reduction potential (IRP) of AWO (−0.27 eV) limits the liberation of superoxide radicals at its CB_{min}. Despite the substantial oxidation potential region of VB_{max} of +3.01 eV in AWO, the hydroxyl radicals alone cannot predominantly drive the MO degradation process, limiting the activity of AWO@Ag. On the other hand, ZIS, with its strong reduction region (CB_{min} at −0.78 eV), predominantly generates superoxide radicals for dye degradation. However, the insufficient oxidation potential (IOP) of ZIS (VB-max at +1.65 V) hinders hydroxyl radical generation. This results in photoelectrons tunneling from the CBmin of AWO@Ag to the VBmax of ZIS via the Ag-shelled NPs, where they are scavenged by the photogenerated holes of ZIS. This phenomenon establishes a Z-scheme heterojunction mediated by Ag, facilitating effective charge separation and recombination process. Similarly, the IRP of AWO@Ag obstructs the reduction of protons from water molecules, rendering AWO inactive for molecular H_2 generation at its CB_{min}. The VB_{max} position of ZIS contains photo-holes with weak oxidation potential (WOP), which

© 2025 Wiley-VCH GmbH

16136829, 2025, 34, Downloaded from https://onlinelibrary.wiley.com/doi/10.1002/smll.202501833 by Jeonbuk National University, Wiley Online Library on [18/10/2026]. See the Terms and Conditions (https://onlinelibrary.wiley.com/terms-and-conditions) on Wiley Online Library for rules of use; OA articles are governed by the applicable Creative Commons License

recombine with photoelectrons from CB_{min} of AWO, further supporting Z-scheme heterojunction. Under light irradiation, the photoactive electrons in the conduction band of ZIS directly participate in the proton reduction, while the protons generated during the water oxidation reaction at the valence band of AWO and ZIS are also actively reduced by the photoactive electrons in the conduction band of ZIS surface. This shows that the active sites of ZIS plays predominant role in photocatalytic H_2 production. Furthermore, the addition of AWO to ZIS is critical for suppressing the electron–hole recombination rates and enhancing water oxidation reactions by providing strong oxidizable photoholes. The work function of metallic Ag (4.0 eV) is lower than that of AWO (4.78 eV) and slightly higher than that of ZIS (3.84 eV). Upon light irradiation, the Ag NPs on the AWO core undergo localized surface plasmon resonance (LSPR), generating hot electrons that transfer to the AWO surface. Thereafter, this entire component (AWO@Ag) has the highest tendency to tunnel electrons from this conduction band into the valence band of ZIS. As a result, the useless photoholes are eliminated and useful photoelectrons are preserved, which maximizes the system's efficiency. The role of the lactic acid in eliminating the photoholes located distant from the surface of ZIS is another crucial factor in maximizing the H_2 production rates of AAZ-3. The superior performances of AAZ-3 in dye degradation and H_2 production compared to pristine AWO and ZIS validate the proposed charge transfer mechanism. This enhanced activity can be attributed to the synergistic interaction of the Ag-shelled AWO core with ZIS nanosheets, effectively suppressing electron–hole recombination and leveraging the strong oxidation capability provided by the Z-scheme heterojunction.

2.5. Post-Photocatalytic Structural and Chemical Integrity Assessment of AAZ-3

Practical deployment of photocatalytic materials demands exceptional durability alongside high performance. Since the long-term viability of photocatalytic systems depends on their chemical stability under operational conditions, we tested and confirmed the stability of our developed core–shell mediated Z-scheme heterojunction (AAZ-3) through prolonged hydrogen evolution and dye degradation experiments, providing empirical evidence.

To support the activities attained during recyclability studies we have collected the photocatalyst material after testing for long hours and washed three times with water, two times with ethanol, and dried overnight at 60 °C. Further, the catalyst was subjected to XRD, FTIR, and XPS analysis. Results obtained were presented in Figures S19–S21 (Supporting Information). Crystallographic analysis conducted at same scan rates as earlier affirms the preserved crystallinity of AAZ-3. X-ray diffraction analysis of the spent AAZ-3 sample (Figure S19, Supporting Information) confirmed remarkable structural stability. The diffraction patterns for fresh and used catalysts exhibited identical peak positions, demonstrating preservation of the crystallographic structure after prolonged photocatalytic operation. All characteristic peaks corresponding to hexagonal $ZnIn_2S_4$ (JCPDS No. 72–0773) and orthorhombic Ag_2WO_4 (JCPDS No. 34–0061) phases remained unchanged, with no emergence of additional peaks or occurrence of abnormal shifts in 2θ positions. The well-maintained peak intensities along with the base and shapes indicated that both crystallinity and phase composition were uncompromised and retained throughout and after the testing. IR spectroscopic results (Figure S20, Supporting Information) of the AAZ-3 sample verified remarkable chemical stability throughout hydrogen evolution testing in 5 vol% lactic acid solutions. All characteristic vibrational signatures remained intact, with the hydroxyl stretching band near 3450 cm^{-1} and water bending mode at 1600 cm^{-1} displaying slightly changed intensities. Critical metal-oxygen framework vibrations, including W—O and W—O—W stretches at 750–800 cm^{-1} and In-S broad modes in the 1100^{-1} range, exhibited no spectral alterations. Significantly, the absence of additional peaks attributable to irreversibly adsorbed lactate or pyruvate species or photocatalytic byproducts confirmed efficient surface regeneration during operation.

Building upon the structural and molecular stability confirmed by XRD and FTIR analyses, surface chemical states of the AAZ-3 were investigated using high-resolution XPS to provide atomic-level insights into compositional integrity. Figure S21 (Supporting Information) (HR-XPS spectra of spent AAZ-3) revealed remarkable chemical stability of the AAZ-3, with negligible binding energy shifts in a majority of the AAZ-3 constituents, while Table S5 (Supporting Information), summarizes the binding energy shifts of all constituent elements before and after photocatalytic activity tests. The difference in binding energies of ZIS constituents is in the order of less than 0.1 eV, with Zn $2p_{3/2}$ ($\Delta = -0.07$ eV), In $3d_{5/2}$ ($\Delta = -0.02$ eV), and S $2p_{3/2}$ ($\Delta = -0.07$ eV) demonstrating retention of their chemical states. In the case of AWO@Ag constituents metallic Ag species showed a minor positive shift (+0.37 eV), while Ag^{+1} maintained its binding energy without noticeable shift, indicating preservation of the Ag as a mediator and AWO component in the Z-scheme architecture.

Notably, W 4f peaks exhibited moderate positive shifts (+0.98 and +0.80 eV), accompanied by oxygen species redistributions. Lattice oxygen decreased slightly (−0.21 eV), while oxygen vacancy species increased (+0.99 eV), and chemisorbed oxygen reduced substantially (−1.32 eV). These coordinated shifts in W and O species suggest surface reconstruction rather than decomposition, likely involving the conversion of chemisorbed oxygen to vacancy states during photocatalysis. The distinct binding energy shifts observed in W 4f HR-XPS spectra provide critical evidence for surface restructuring at the oxidation sites. As AWO serves as the oxygen evolution photocatalyst, its direct interaction with lactic acid (sacrificial electron donor) induces notable changes. The systematic conversion of chemisorbed oxygen (−1.32 eV) to oxygen vacancies (+0.99 eV) attributed to the lactic acid consumption of photogenerated holes promotes surface dehydroxylation. The significantly larger shift in W 4f corresponding to AWO of OEP component than those of $ZnIn_2S_4$ components, demonstrates selective adaptation at oxidation sites where hole transfer occurs. The metallic Ag mediator maintained electronic conductivity with minimal perturbation (+0.37 eV), ensuring efficient charge shuttling between semiconductors, which further supports the proposed mechanism in Figure 9. Collectively, these differential binding energy shifts reveal a self-optimizing mechanism where the Z-scheme architecture adapts primarily at the oxidation interface while preserving the reduction centers. This demonstrates adaptive surface chemistry

© 2025 Wiley-VCH GmbH

16136829, 2025, 34, Downloaded from https://onlinelibrary.wiley.com/doi/10.1002/smll.202501833 by Jeonbuk National University, Wiley Online Library on [18/10/2026]. See the Terms and Conditions (https://onlinelibrary.wiley.com/terms-and-conditions) on Wiley Online Library for rules of use; OA articles are governed by the applicable Creative Commons License

without compromising core structure of AWO facilitated by the shelling of Ag. Thus, Ag shell accomplishes its crucial role in mediating intrinsic Z-scheme recombination between photogenerated electrons from AWO conduction band and holes from ZIS valence band. explaining the sustained photocatalytic performance despite surface modifications during continuous operation underscoring the robust structural integrity of the heterojunction architecture under operational conditions.

3. Conclusion

In this study, a systematic approach has been proposed and successfully developed by constructing a core–shell integrated Z-scheme mediated heterojunction. Instead of directly coupling oxidation and reduction components, we introduced Ag shelling over a wide bandgap semiconductor (AWO) to form a core–shell structure (AWO@Ag), which effectively suppresses overall electron–hole recombination. This distinctive approach facilitated the formation of LSPR-assisted visible light responsive AWO@Ag, enabling hot electron injection and continuous cocatalyst (Ag) intercalation with multiple electron transfer sites. The AWO@Ag structure was subsequently integrated with ZIS nanosheets and optimized for photocatalytic and photoelectrochemical properties. By determining the optimal loading of AWO@Ag over ZIS surface, it was found that the H_2 production rate for the AAZ-3 photocatalyst was enhanced to 3142 µmol h^{-1} g^{-1} using a small amount (5 vol.%) of lactic acid. This enhancement was a 2.36 folds increase compared to pristine ZIS (1311 µmol h^{-1} g^{-1}) under identical testing conditions. Furthermore, the optimized AAZ-3 photocatalyst exhibited an exceptional dye degradation efficiency of 97.16% within 1 h against a high concentration (20 ppm) of methyl orange dye. Additionally, the photocatalyst exhibited excellent PEC water oxidation performance, achieving a photocurrent density of 3.91 mA cm^{-2} at 2.2 V versus RHE. Moreover, the incorporation of metallic Ag not only enhanced the light absorption capabilities and suppressed the electron–hole recombination rates but also improved excellent stability and performance, surpassing other ZIS-based photosystems. Consequently, the manifested AWO@Ag/ZIS system exhibits multifunctional behavior and introduces a notable and unique core–shell mediated Z-scheme heterojunction structure strategy with the potential in effective utilization of wide bandgap semiconductors. We believe this strategy can lead to design and development of stable and efficient photocatalytic systems, serving as a new technique for green and clean fuel genration. This research has the potential to inspire further exploration and innovation in the fields of photocatalysis and materials science.

4. Experimental Section

Synthesis of Ag_2WO_4, Ag/Ag_2WO_4 and Ag_2WO_4@Ag: The present work adopted a conventional hydrothermal route to synthesize silver tungstate nanostructures. Silver nitrate ($AgNO_3$, 99.0% purity, Sigma Aldrich) and sodium tungstate dihydrate ($Na_2WO_4 \cdot 2H_2O$, 99.5% purity, Sigma Aldrich) were used as precursor materials. At first 3 mmol of aqueous silver precursor was prepared with 40 mL of Millipore water and kept for stirring at 500 rpm for 5 min. Meanwhile sodium precursor of 1.5 mmol in 40 mL of Millipore water and kept for stirring at same rpm for 10 min until the solution became transparent. Further, the silver precursor solution was added dropwise to the tungsten precursor using a pump setup at a rate of 15–20 drops per minute. The complete transfer took ≈1 h, followed by an additional 30 min of stirring to ensure homogeneity of the dispersion. All three silver tungstate variants were prepared at 180 °C for 24 h condition in 100 mL hydrothermal autoclave.

For the synthesis of pristine Ag_2WO_4, SDS (sodium dodecyl sulfate) was used as a surfactant. Prior to the addition of the Ag precursor solution, 1 g of SDS was added to the sodium tungstate solution and stirred for 30 min. The pH of the as-prepared mixture was found to be 8 ± 0.5 and was adjusted to 9 using 0.1 M NaOH solution. The entire reaction mixture was transferred and tightly sealed to prevent leakage within the autoclave and kept in an oven. For Ag-loaded Ag_2WO_4 (Ag/Ag_2WO_4), the aforementioned protocol was repeated, with the addition of 0.1 g of polyvinylpyrrolidone (PVP) to the silver precursor solution. Specifically, the PVP addition was performed before adding silver nitrate to SDS contained sodium tungstate solution, and the rest of the method was the same as the pristine silver tungstate synthesis.

For Ag-shelled Ag_2WO_4 synthesis, the intrinsic nucleation nature of silver tungstate was preserved by adding a small amount of oxalic acid (0.1 mmol) to the 40 mL aqueous sodium tungstate solution. The addition of PVP was conducted in the same manner as for Ag/Ag_2WO_4. In all three cases, after completing the reaction, the autoclave was allowed to cool naturally. Further, the contents were collected and thoroughly washed with Millipore water three times with 50 mL of water. Subsequently, the solution was washed twice with 50 mL of ethanol and centrifuged. The final product was collected and dried at 60 °C followed by grinding into a fine powder for further use. The pristine Ag_2WO_4 was denoted as AWO, and Ag NPs doped Ag_2WO_4 was labeled as Ag/AWO, and uniformly Ag-shelled Ag_2WO_4 was designated as AWO@Ag. The methodologies of pristine AWO, Ag/AWO, and AWO@Ag are detailed in a flow chart presented in Figure S1 (Supporting Information).

Synthesis of $ZnIn_2S_4$ Nanosheets (ZIS): ZIS nanosheets were prepared through a hydrothermal approach using a precursor ratio of Zinc (Zn): Indium (In): Sulfur (S) as 1:2:4. Briefly, 5, 10 and 20 mmol of zinc nitrate ($Zn(NO_3)_2 \cdot 6H_2O$, 98%, ACS reagent), indium chloride ($InCl_3$, 98%, Sigma Aldrich), thioacetamide (C_2H_5NS, 99%, Sigma Aldrich), respectively. First, all three precursors were dissolved in 50 mL of Milli Q water (resistivity: 18.2 MΩ) and stirred for 30 min. The mixture was then transferred to a stainless teal autoclave with Teflon container. The reactor was sealed and hydrothermally treated at 180 °C for 24 h. Further, the washing procedure was identical to that used for silver tungstate synthesis; washing twice with water, once with anhydrous ethanol, and then dried at 60 °C for 12 h. The final product, a yellow-colored, talc-like powder, was labeled as ZIS and stored for further use.

Synthesis of (AWO@Ag)-ZIS (AAZ) Ternary Composites: As prepared ZIS and AWO@Ag were accurately weighed. Different weight percentages (wt.%) of AWO (7.5, 10, 12.5, 15, 17.5) were loaded onto ZIS using a wet impregnation approach. For the preparation of AAZ-3, 25 mg of AWO@Ag and 175 mg of ZIS were individually weighed and dispersed in ethanol (25 mg AWO@Ag in 25 mL EtOH, 175 mg ZIS in 75 mL EtOH) with the respective volumes to prepare their aqueous solutions. Each of these aqueous solutions was sonicated for 30 min and then stirred for 1 h. The AWO solution was then added dropwise to ZIS, and the reaction mixture was further sonicated for 1 h. The final mixture was heated at 60 °C to completely evaporate the solvent (EtOH), which took ≈200–220 min. Then, the formed solids were further dried in a preheated oven at 100 °C for 1 h to remove residual solvent. After cooling naturally to room temperature, the material was ground into fine powders, labeled as AAZ-3, and stored for further use. All other ternary composites (AAZ-1, 2, 4 & 5) were also prepared using the same method with their respective weights.

Photocatalytic and Photoelectrochemical Measurements–Dye Degradation: Methyl orange (MO, Sigma Aldrich, certified 95% dye content) was used to prepare a 20 ppm dye solution with Milli Q water (18.2 MΩ). The dye solution without catalyst was tested under dark condition and light irradiation (λ = 380–740 nm) to evaluate its degradation. Irradiation of the 20 ppm MO dye solution for 1 h resulted in negligible photolysis (<1%).

© 2025 Wiley-VCH GmbH

16136829, 2025, 34, Downloaded from https://onlinelibrary.wiley.com/doi/10.1002/smll.202501833 by Jeonbuk National University, Wiley Online Library on [18/10/2026]. See the Terms and Conditions (https://onlinelibrary.wiley.com/terms-and-conditions) on Wiley Online Library for rules of use; OA articles are governed by the applicable Creative Commons License

For photocatalytic dye degradation testing, 50 mg of catalyst was added to 50 mL 20 ppm dye solution in a round bottom flask, which was covered completely with aluminum foil to create a dark environment. A dark condition run was performed using a magnetic stirrer, and the adsorption-desorption equilibrium times were monitored and the optimal time was found to be 40 min. An aliquot of the sample was taken and tested prior to light irradiation. The result was found to be the same as in the case of photolysis of dye, meaning that there was no appreciable degradation under dark condition. The entire reaction mixture was irradiated with visible light (Asahi Spectra, MAX 303, Xenon lamp, Power 220 mW Cm^{-2}). Samples (1.5 ± 0.1 mL) were collected every 10 min from the reactor, and the degradation rate was assessed using UV–vis spectrophotometry (at λ = 464 nm). The optical density values were obtained from the absorbance spectra at the maximum wavelength (λ_{max}). The degradation rate (%) was calculated using the formula:

$$\text{Degradationrate}\ (\%) = (C_0 - C_t / C_0)\ 100\% \quad (2)$$

where C_0 and C_t represent the initial concentration of the MO (at 0 min) and the concentration at time t (min), respectively (t = 10, 20, 30, 40, 50, and 60 min).

H_2 Generation: Photocatalytic HER evaluations were performed in a 180 mL quartz-made Kjeldahl flask as reported earlier.[28] The reactor was filled with 5 vol.% lactic acid containing 50 mL milli Q water, which was purged with nitrogen gas, and then 10 mg of accurately weighed catalyst was added. The reactor was sealed with an airtight rubber septum and wrapped with Teflon tape to prevent leakage. The testing procedure can be classified into three different steps. First, the solution was stirred under dark conditions to attain dispersion and adsorption-desorption equilibrium for 15 min. Next, the reaction mixture was evacuated with a pump (GAST, DOA-P704-AA) for 15 min to remove the gaseous contents and create an inert ambience inside the reactor. Finally, the reaction mixture was bubbled with ultra-high pure nitrogen (purging) to remove the dissolved oxygen in the reaction mixture. After this step, the excessive pressure was removed, the purged reaction mixture is tested and the absence of dissolved oxygen was ensured from the peak-free chromatogram (GC-2010, Shimadzu, equipped with TCD detector, N_2 as carrier gas, flow rate of 25 ml/min). The reactor was irradiated with light for 4 continuous hours, and H_2 evolution was analyzed hourly. The average H_2 evolution rate over 4 h was calculated to ensure accuracy.

Photoelectrochemical Water Splitting: The oxygen evolution (OER) reaction rates of the prepared catalysts were analyzed through PEC analysis. A conventional three-electrode system containing a quartz cell was used for testing. Pt foil (1 cm x 2 cm) was used as a counter electrode, a photo-catalyst coated on FTO glass was used as the working electrode, and Ag/AgCl (saturated KCl) was used as a reference electrode. 10 mL of catalyst ink was prepared using 5:1 ratio solution of IPA and Nafion (0.02%) with 5 mg of the catalyst. The prepared solution was coated on the conductive side of FTO glass for 10 cycles at 3000 rpm using a spin coating instrument. After each coating cycle, the substrate was dried on a hot plate for 5 min. Further, the coated FTO was dried in a preheated oven at 100 °C for 6 h. Thoroughly cleaned neat FTO was analyzed under the same conditions as the coated ones, but the FTO electrode without catalyst exhibited negligible current densities. For testing PEC activity, 0.5 M Na_2SO_4 is used as an electrolyte with a pH near neutral. For pristine and binary composite samples, cyclic voltammograms (CV) were collected at a scan rate of 50 mV s^{-1} and analyzed to understand the HER and OER capabilities of the as prepared photocatalysts. OER LSV plots were collected at 10 mV/s. M-S plots were collected at 500, 1000, and 1500 Hz. EIS responses were collected at frequencies between 10^5 to 0.01 Hz under open circuit conditions.

Supporting Information

Supporting Information is available from the Wiley Online Library or from the author.

Acknowledgements

This work was supported by 1) BK21-FOUR programs of the Ministry of Education and Human-Resource Development, South Korea, and the National Research Foundation of Korea (NRF), 2) the Commercialization Promotion Agency for R&D Outcomes (COMPA) grant funded by the Korea government (Ministry of Science and ICT) (RS-2025-02314407) and 3) the Regional Innovation System & Education (RISE) initiative, funded by the Ministry of Education and administered by the National Research Foundation of Korea (NRF).

Conflict of Interest

The authors declare no conflict of interest.

Data Availability Statement

The data that support the findings of this study are available from the corresponding author upon reasonable request.

Keywords

Ag-shelled Ag_2WO_4, H_2 production, plasmonic hot spots, $ZnIn_2S_4$, Z-scheme

Received: February 12, 2025
Revised: May 14, 2025
Published online: June 27, 2025

[1] L. Lin, Y. Ma, J. J. M. Vequizo, M. Nakabayashi, C. Gu, X. Tao, H. Yoshida, Y. Pihosh, Y. Nishina, A. Yamakata, N. Shibata, T. Hisatomi, T. Takata, K. Domen, *Nat. Commun.* **2024**, *15*, 397.
[2] Y. Chen, K. Dong, L. Amirav, *Chem. Mater.* **2022**, *34*, 9373.
[3] S. Chen, T. Takata, K. Domen, *Nat. Rev. Mater.* **2017**, *2*, 1.
[4] M. P. Ravikumar, S. Bharathkumar, B. Urupalli, M. K. Murikinati, S. M. Venkatakrishnan, S. Mohan, *Energy and Fuels* **2022**, *36*, 11503.
[5] U. Bharagav, N. R. Reddy, V. Nava Koteswara Rao, P. Ravi, M. Sathish, D. Rangappa, K. Prathap, C. Shilpa Chakra, M. V. Shankar, L. Appels, T. M. Aminabhavi, R. R. Kakarla, M. M. Kumari, *Chemosphere* **2023**, *311*, 137030.
[6] A. Vilanova, P. Dias, T. Lopes, A. Mendes, *Chem. Soc. Rev.* **2024**, *53*, 2388.
[7] D. Gunawan, J. Zhang, Q. Li, C. Y. Toe, J. Scott, M. Antonietti, J. Guo, R. Amal, *Adv. Mater.* **2024**, *2404618*, 1.
[8] L. Quan, H. Jiang, G. Mei, Y. Sun, B. You, *Chem. Rev.* **2024**, *124*, 3694.
[9] H. Song, S. Luo, H. Huang, B. Deng, J. Ye, *ACS Energy Lett.* **2022**, *7*, 1043.
[10] J. Panda, P. Behera, S. Subudhi, S. P. Tripathy, G. Swain, S. Dash, K. Parida, *Mater. Adv* **2024**, *5*, 4865.
[11] W. K. Chong, B. J. Ng, L. L. Tan, S. P. Chai, *Energy and Fuels* **2022**, *36*, 4250.
[12] G. Swain, S. Sultana, K. Parida, *Inorg. Chem.* **2019**, *58*, 9941.
[13] J. Sahu, B. P. Mishra, K. Parida, *ACS Appl. Energy Mater.* **2025**, *8*, 388.
[14] X. Xin, Y. Li, Y. Zhang, Y. Wang, X. Chi, Y. Wei, C. Diao, J. Su, R. Wang, P. Guo, J. Yu, J. Zhang, A. J. Sobrido, M. M. Titirici, X. Li, *Nat. Commun.* **2024**, *15*, 1.
[15] Y. Zheng, Y. Wang, S. Mansoor, Z. Hu, Y. Zhang, Y. Liu, L. Zhou, J. Lei, J. Zhang, *Small* **2024**, *20*, 2311725.
[16] B. Han, Y. H. Hu, *Energy Sci. Eng.* **2016**, *4*, 285.
[17] L. Que, L. Lu, Y. Xu, X. Xu, H. Li, J. Cao, M. Zhu, C. Li, J. Pan, *Int. J. Hydrogen Energy* **2023**, *48*, 4708.

© 2025 Wiley-VCH GmbH

16136829, 2025, 34, Downloaded from https://onlinelibrary.wiley.com/doi/10.1002/smll.202501833 by Jeonbuk National University, Wiley Online Library on [18/10/2026]. See the Terms and Conditions (https://onlinelibrary.wiley.com/terms-and-conditions) on Wiley Online Library for rules of use; OA articles are governed by the applicable Creative Commons License

[18] S. Si, H. Shou, Y. Mao, X. Bao, G. Zhai, K. Song, Z. Wang, P. Wang, Y. Liu, Z. Zheng, Y. Dai, L. Song, B. Huang, H. Cheng, *Angew. Chem., Int. Ed.* **2022**, *61*, 202209446.
[19] P. Dong, T. Cheng, J. L. Zhang, J. Jiang, L. Zhang, X. Xi, J. Zhang, *ACS Appl. Energy Mater.* **2023**, *6*, 1103.
[20] W. Shi, B. Ge, P. Jiang, Q. Wang, L. He, C. Huang, *Appl. Catal. B Environ.* **2024**, *354*, 124121.
[21] Y. Wang, W. Huang, S. Guo, X. Xin, Y. Zhang, P. Guo, S. Tang, X. Li, *Adv. Energy Mater.* **2021**, *11*, 2102452.
[22] S. Ding, I. Medic, N. Steinfeldt, T. Dong, T. Voelzer, S. Haida, J. Rabeah, J. Hu, J. Strunk, *Small Struct.* **2023**, *4*, 2300091.
[23] Y. H. Li, M. Y. Qi, Z. R. Tang, Y. J. Xu, *J. Phys. Chem. C* **2022**, *126*, 1872.
[24] W.-K. Chong, B.-J. Ng, X. Y. Kong, L.-L. Tan, L. K. Putri, S.-P. Chai, *Appl. Catal. B Environ.* **2023**, *325*, 122372.
[25] H. Fan, Y. Jin, K. Liu, W. Liu, *Adv. Sci.* **2022**, *9*, 2104579.
[26] X. Niu, X. Bai, Z. Zhou, J. Wang, *ACS Catal.* **2020**, *10*, 1976.
[27] Y. Wang, H. Suzuki, J. Xie, O. Tomita, D. J. Martin, M. Higashi, D. Kong, R. Abe, J. Tang, *Chem. Rev.* **2018**, *118*, 5201.
[28] U. Bharagav, N. R. Reddy, V. N. Koteswararao, P. Ravi, K. Pratap, M. Sathish, K. K. Cheralathan, M. V. Shankar, M. M. Kumari, *Energy and Fuels* **2020**, *34*, 14598.
[29] J. Zhang, X. Sun, J. Ma, Z. Yi, T. Xian, S. Wang, G. Liu, X. Wang, H. Yang, *Appl. Surf. Sci.* **2023**, *611*, 155681.
[30] A. Sabbah, I. Shown, M. Qorbani, F. Y. Fu, T. Y. Lin, H. L. Wu, P. W. Chung, C. I. Wu, S. R. M. Santiago, J. L. Shen, K. H. Chen, L. C. Chen, *Nano Energy* **2022**, *93*, 106809.
[31] R. O. Mohammed, A. A. Amooey, S. H. Ammar, M. D. Salman, *J. Taiwan Inst. Chem. Eng.* **2023**, *151*, 105141.
[32] P. Zhou, A. Zhang, D. Zhang, C. Feng, S. Su, X. Zhang, J. Xiang, G. Chen, Y. Wang, *Chem. Eng. J.* **2019**, *373*, 780.
[33] J. Lv, K. Dai, J. Zhang, L. Lu, C. Liang, L. Geng, Z. Wang, G. Yuan, G. Zhu, *Appl. Surf. Sci.* **2017**, *391*, 507.
[34] L. Zhou, Y. Li, S. Yang, M. Zhang, Z. Wu, R. Jin, Y. Xing, *Chem. Eng. J.* **2021**, *420*, 130361.
[35] L. Zhang, Z. Wang, C. Hu, B. Shi, *J. Colloid Interface Sci.* **2019**, *553*, 598.
[36] M. Pirhashemi, A. Habibi-Yangjeh, *J. Colloid Interface Sci.* **2017**, *491*, 216.
[37] J. Huang, D. Li, Y. Liu, R. Li, P. Chen, H. Liu, W. Lv, G. Liu, Y. Feng, *J. Hazard. Mater.* **2020**, *392*, 122355.
[38] Y. Li, Y. Li, S. Ma, P. Wang, Q. Hou, J. Han, S. Zhan, *J. Hazard. Mater.* **2017**, *338*, 33.
[39] Y. Li, R. Jin, X. Fang, Y. Yang, M. Yang, X. Liu, Y. Xing, S. Song, *J. Hazard. Mater.* **2016**, *313*, 219.
[40] S. Balasurya, M. K. Okla, I. A. Alaraidh, W. Soufan, A. A. AL-ghamdi, S. R. Ahamad, M. A. Abdel-Maksoud, H. AbdElgawad, L. L. Raju, A. M. Thomas, S. S. Khan, *Chemosphere* **2022**, *297*, 134130.
[41] N. G. Macedo, A. F. Gouveia, R. A. Roca, M. Assis, L. Gracia, J. Andrés, E. R. Leite, E. Longo, *J. Phys. Chem. C* **2018**, *122*, 8667.
[42] H. Liu, F. Sun, X. Li, Q. Ma, G. Liu, H. Yu, W. Yu, X. Dong, Z. Su, *Compos. Part B Eng.* **2023**, *259*, 110746.
[43] A. M. Elgorban, A. A. Al Kheraif, A. Syed, *Colloids Surfaces A Physicochem. Eng. Asp.* **2021**, *629*, 127416.
[44] J. Wang, D. Wang, X. Zhang, C. Zhao, M. Zhang, Z. Zhang, J. Wang, *Int. J. Hydrogen Energy* **2019**, *44*, 6592.
[45] B. Wang, Z. Deng, X. Fu, Z. Li, *J. Mater. Chem. A* **2018**, *6*, 19735.
[46] X. Peng, J. Li, L. Yi, X. Liu, J. Chen, P. Cai, Z. Wen, *Appl. Catal. B Environ.* **2022**, *300*, 120737.
[47] M. M. Mohamed, H. El-Farsy, *Sci. Rep.* **2020**, *10*, 21495.
[48] Z. Xu, W. Shi, Y. Shi, H. Sun, L. Li, F. Guo, H. Wen, *Appl. Surf. Sci.* **2022**, *595*, 153482.
[49] W.-K. Chong, B.-J. Ng, Y. J. Lee, L.-L. Tan, L. K. Putri, J. Low, A. R. Mohamed, S.-P. Chai, *Nat. Commun.* **2023**, *14*, 7676.
[50] Y. Ding, Y. Chen, Z. Guan, Y. Zhao, J. Lin, Y. Jiao, G. Tian, *ACS Appl. Mater. Interfaces* **2022**, *14*, 7888.
[51] C. Zhang, K. Gao, H. Zhu, J. Liu, J. Chen, F. Xie, W. Xie, X. Wang, *ChemCatChem* **2022**, *14*, 1.
[52] S. Kokilavani, A. Syed, M. Raaja Rajeshwari, V. Subhiksha, A. M. Elgorban, A. H. Bahkali, N. S. S. Zaghloul, A. Das, S. S. Khan, *J. Alloys Compd.* **2022**, *889*, 161662.
[53] U. Bharagav, N. R. Reddy, V. N. Rao, P. Ravi, M. Sathish, M. V. Shankar, T. M. Aminabhavi, R. R. Kakarla, M. M. Kumari, *Chem. Eng. J.* **2023**, *465*, 142886.
[54] Y. Li, S. Li, L. Meng, S. Peng, *J. Colloid Interface Sci.* **2023**, *650*, 266.
[55] Y. Jiang, S. Pillai, M. A. Green, *Sci. Rep.* **2016**, *6*, 1.
[56] M. S. Bin-Alam, O. Reshef, Y. Mamchur, M. Z. Alam, G. Carlow, J. Upham, B. T. Sullivan, J. M. Ménard, M. J. Huttunen, R. W. Boyd, K. Dolgaleva, *Nat. Commun.* **2021**, *12*, 974.
[57] U. Bharagav, N. R. Reddy, V. N. Rao, P. Ravi, M. Sathish, M. V. Shankar, M. M. Kumari, *Int. J. Hydrogen Energy* **2022**, *47*, 40391.
[58] M. P. Ravikumar, T. A. Quach, B. Urupalli, K. Manjunatha, M. K. Murikinati, S. M. Venkatakrishnan, S. Y. Wu, T. O. Do, S. Mohan, *ACS Sustainable Chem. Eng.* **2023**, *11*, 17272.
[59] L. R. Nagappagari, T. D. Le, M. J. Ahemad, G.-J. Oh, G.-S. Shin, K. Lee, Y.-T. Yu, *Mater. Today Nano* **2023**, *22*, 100325.
[60] M. Singh, T. P. Rugma, S. Golda A, B. Neppolian, M.u. Naushad, S. K. Lakhera, *J. Clean. Prod.* **2024**, *442*, 140921.
[61] Y. Su, H. Xiong, L. Liao, H. Lei, Z. Wang, H. Chen, H. Xu, Y. Pan, W. Yu, X. Xiong, Q. Li, K. Gu, L. Yao, J. Zhao, W. Mai, *Nano Energy* **2024**, *127*, 109747.
[62] D. Y. Um, B. Chandran, J. K. Oh, S. U. Kim, Y. T. Yu, J. H. Park, C. R. Lee, Y. H. Ra, *Chem. Eng. J.* **2023**, *472*, 144997.
[63] D. Wang, P. Bassi, H. Qi, X. Zhao, Gurudayal, L. W., R. Xu, T. Sritharan, Z. Chen, *Materials (Basel)* **2016**, *9*, 348.
[64] Z. Bao, Y. Jiang, Z. Zhang, J. Lv, W. Shen, J. Dai, J. Wang, J. Cai, Y. Wu, *J. Mater. Chem. A* **2024**, *12*, 15902.
[65] Z. Guan, Z. Xu, Q. Li, P. Wang, G. Li, J. Yang, *Appl. Catal. B Environ.* **2018**, *227*, 512.
[66] L. Paramanik, L. Mohapatra, D. Y. Choi, S. H. Yoo, *Compos. Part B Eng.* **2024**, *278*, 111416.

© 2025 Wiley-VCH GmbH

16136829, 2025, 34, Downloaded from https://onlinelibrary.wiley.com/doi/10.1002/smll.202501833 by Jeonbuk National University, Wiley Online Library on [18/10/2026]. See the Terms and Conditions (https://onlinelibrary.wiley.com/terms-and-conditions) on Wiley Online Library for rules of use; OA articles are governed by the applicable Creative Commons License